MODELING DISTRIBUTED ROUGHNESS USING EFFECTIVE SURFACES

A Thesis

by

MADELINE NICOLE MCMILLAN

Submitted to the Office of Graduate and Professional Studies of
Texas A&M University
in partial fulfillment of the requirements for the degree of

MASTER OF SCIENCE

Chair of Committee,	Edward White
Committee Members,	Helen Reed
	Prabir Daripa
Head of Department,	Rodney Bowersox

December 2019

Major Subject: Aerospace Engineering

ABSTRACT

How laminar flow interacts with distributed roughness has yet to be described in a cohesive fashion. To advance theoretical efforts, a preliminary model inspired by experimental results is proposed here and evaluated. Significant evidence suggests distributed roughness fields generate a 'shielding' effect that reduces the impact of individual roughness elements on the flow. One way to model shielding is to create an effective surface which reduces the apparent height of the roughness elements. In this thesis, possible effective surfaces are coupled with different wall boundary conditions. These are analyzed using triple-deck theory. The results are examined for their effectiveness at reproducing results from a full distributed roughness configuration. Results from this effort have discounted no-shear as a possible boundary condition. Furthermore, a simplified imposed-slip velocity model demonstrates the strong dependence of the model's success upon matching actual in-plane velocity values where the effective surface replaces the control geometry.

DEDICATION

This work is for my parents. Thank you for always believing in me.

CONTRIBUTORS AND FUNDING SOURCES

Contributors

Funding Sources

TABLE OF CONTENTS

LIST OF FIGURES

1. INTRODUCTION

Boundary layer transition is an important field of study in aerodynamics. Whether a boundary layer is laminar or turbulent has a large impact on vehicle performance due to increases in both surface drag and heating. These increases can happen suddenly when imperfections on an aerodynamic body cause unexpected transition. Understanding how boundary layers are destabilized and become turbulent enhances engineers' ability to design for realistic flight conditions. Accurately modeling real world scenarios, such as roughness present on a wing, requires in-depth research on the various paths to transition.

Historical understanding of boundary layer transition mechanisms was limited to what was described by linearized stability theory and what was not. Linear stability theory utilizes the Orr-Sommerfeld equation, which considers how infinitesimal disturbances in a parallel flow grow or decay. While powerful, the Orr-Sommerfeld equation is limited by the assumptions imposed during its derivation. Larger perturbations of the undisturbed 'basic state' flow can bypass the mechanisms predicted by linear theory and cause early transition. The distinction between a linear stability regime and a bypass regime was augmented by the introduction of the idea of transient growth (Fig. 1.1). Transient growth analytically attributes the brief algebraic growth and subsequent exponential decay of disturbance energy to the superposition of non-orthogonal, stable modes [3]. The transition process is initiated by receptivity, which describes the process by which disturbances that are present in the environment are introduced into the boundary layer. This is the initial value portion of the transition problem.

A common environmental disturbance found on aerodynamic vehicles is surface roughness. Surface roughness can be broken up into several different categories: 2D (spanwise invariant) roughness such as steps between panels, isolated 3D discrete roughness elements (DREs), and distributed 3D roughness. For 2D roughness and DREs, transition can be empirically captured through a roughness-based Reynolds number $Re_{kk} = kU(k)/\nu$, where k is the roughness height and $U(k)$ is the undisturbed velocity at the height of the roughness [4]. However, for distributed
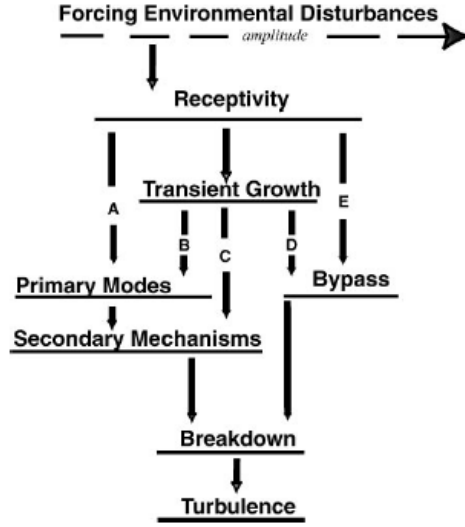
Figure 1.1: Transition Roadmap (Reprinted from [1])

roughness, no good models or correlations exist.

Unlike distributed roughness, the transition mechanisms involving 2D and 3D isolated roughness are somewhat well understood. The process begins with receptivity, where the roughness elements set the amplitude of the disturbances introduced into the flow. The presence of 2D roughness greatly amplifies the existing Tollmien-Schlichting (TS) waves through inflectional velocity profiles in the separated region immediately downstream of the element. This can cause premature transition [5]. DREs affect transition through a different mechanism. Close examination of the vortex structure caused by a DRE reveals a horseshoe vortex wrapping around the DRE. As Re_{kk} exceeds 300, secondary hairpin vortices are shed from the unsteady shear layer immediately above the separated region behind the roughness element [5]. These vortices move high-speed fluid into the low-speed regions, and vice-versa, contributing to a 'lift-up' mechanism that increases disturbance energy, even if the vortices themselves are stable. This growth in disturbance energy is captured in the linear growth predicted by transient growth theory [6].

The mechanisms responsible for transition due to distributed 3D roughness elements are less apparent. While many attempts have been made to find the connection between predictive models for discrete roughness and distributed roughness, the two differ greatly because the boundary layer

2

does not interact with single roughness elements in isolation when encountering a roughness field. Evidence suggests that linear superposition of the effects of individual roughness features is not possible; this is one of the fundamental challenges of distributed roughness.

Close examination of distributed roughness to further investigate other possible mechanisms presents several difficulties for both experimentalists and computationalists. Examining flow very near the roughness field requires unconventional experimental methods or prohibitively high computational costs for direct numerical simulations. The overall problem is further complicated by the large parameter space that is needed to fully characterize randomly rough surfaces. Developing a simpler computational model would aid in understanding how laminar flow interacts with distributed roughness fields by identifying important parameters and simplifying calculations of distributed roughness elements. A review of distributed roughness literature provides a possible modeling method.

1.1 Background

An early theoretical attempt to explain premature transition due to distributed roughness was made by Singh and Lumley [7]. They considered roughness that had small heights and slopes and calculated the effect of the roughness on the mean flow. Their work indicated the existence of an inflection point within the viscous region very near the wall. However, the outer profile was deemed more stable than a smooth-wall flow due to the boundary layer's higher curvature near the critical layer. To explain experimental evidence that distributed roughness is destabilizing and promotes transition, they argued there must be some wavenumbers that confer energy to the flow at wavelengths which are destabilizing for the profile. This work became inspiration for several other experiments that followed which searched for the predicted inflection point.

Leventhal and Reshotko [8] experimented on distributed roughness fields by measuring above sheets of sandpaper roughness. Inspired by Singh and Lumley, their primary interest was investigating if a mean profile change was responsible for the premature transition caused by distributed roughness. The sheets of sandpaper had leading edge Re_{kk} values of 23 and 192 for the fine and coarse sandpaper, respectively. The fine sandpaper did not cause transition and the boundary lay-

ers above the field were easily fit to a Blasius boundary layer profile. The first few measurements above the coarser roughness could also be fit with a Blasius boundary layer if the no-slip surface was adjusted to lie within the roughness heights. However, transition did occur at downstream stations over the roughness field at a Re_x much sooner than predicted by linear theory and in the free-roughness tests. This indicates that different mechanisms were responsible for transition for the fine- and course-sandpaper tests. Measurements of growing frequencies that lay below the neutral curve were later identified as evidence of transient growth [3].

Pursuing an alternate explanation for distributed roughness effects, Kendall [9] examined the impact of several types of roughness (discrete and distributed) on mean velocity profiles. By measuring the velocity deficit in the wake behind various combinations of roughness elements, he attempted to find support for the idea of linearly superposing roughness wakes to describe the effect of distributed roughness. These experiments were performed on roughness elements that were small compared to the boundary layer thickness but had sufficiently large Re_{kk} that they could accelerate transition. He presented several important findings. First, he noted that the presence of ordered distributed roughness surrounding a DRE reduced the velocity deficit measured aft of the elements. He attributed this effect to the wakes of the distributed roughness sheltering the DRE. Second, when measuring profiles directly above distributed roughness, he noted a displacement of the fluid all along the field. When measuring above the ordered distributed roughness field, the boundary layer could be represented by a Blasius profile shifted outwards. The shift was larger than could be accounted for by the average volumetric presence of the distributed roughness. Finally, after calculating the stability of the mean boundary layer immediately behind the distributed roughness field, it was shown to be more unstable to TS waves than a Blasius boundary layer, however the profile quickly returned to a Blasius profile downstream of the field.

Tadjfar et al. [10] used laser anemometry to study flow near the wall around the same ordered roughness array used by Kendall [9]. They were seeking evidence of more efficient momentum transfer to explain the early transition. In their analysis, they describe the boundary layer as broken into two regions: the outer portion of the boundary layer which did not change in relation to

4

its position above the roughness array, and an inner portion of the profile that did change. In their calculation of shape factor, they linearly extrapolated the inner portion of the profile, and found that the boundary layer origin lay anywhere between 50-90% of the roughness height. They saw repeatable momentum transfer patterns, likely due to the ordered nature of the distributed roughness array they used. Tadjfar et al. state that there was no evidence found for TS instability waves in their experiment.

Corke, Bar-Sever, and Morkovin [11] performed an experiment designed explicitly to observe enhanced TS wave growth, using distributed roughness in regions where $Re_{\delta*} > Re_{\delta*,crit}$. They placed a large field of distributed roughness slightly recessed into the wall to prevent the lip of the roughness from triggering 2D transition mechanisms. After extensive hot-wire measurements and smoke-wire visualization tests, they concluded that the distributed roughness does enhance the growth of TS waves, although no inflection point near the roughness was observed. They attributed this growth the low-inertia fluid trapped in the roughness valleys having a higher susceptibility to freestream disturbances. Interestingly, they could not correlate the initial onset of turbulent spots with the spanwise position of the highest roughness peaks in the field.

More recently, Downs et al. [12] examined small patches of distributed roughness in the interest of finding evidence of transient growth. The roughness field was examined at three different Re_{kk} configurations, with the lower two ($Re_{kk} = 164, 227$) remaining laminar and the highest ($Re_{kk} = 301$) becoming turbulent. All cases exhibited evidence of transient growth in the disturbance energy. The transitional case did not exhibit evidence of transition due to TS waves, unlike the Corke et al. experiment [11]. However, the type of distributed roughness may have impacted this, as the roughness used by Downs et al. had a much smaller stream- and spanwise extent.

Drews [13] conducted a follow-up study to Downs et al. [12] using DNS and examined vortex structures in the near field wake of the roughness. After matching the results found by Downs et al., Drews investigated some unusual geometry configurations. First, he replaced geometry with negative heights with a surface that allowed velocity slip at the $y = 0$ plane. When comparing the new geometry with velocity measurements from the original velocity at the same height, he found there

was negligible difference. Additionally, disturbance results downstream of the roughness matched well with the original results. Simulating only the tallest roughness elements (removing the smallest roughness peaks and all valleys) caused disturbance energy levels to increase as compared to the full roughness geometry, with higher growth rates immediately downstream of the roughness. This is surprising because a theory built on linear superposition of roughness effects would predict the disturbance energies to decrease. Finally, he found that superposing different roughness together did not yield correct quantitative results, although qualitatively the results matched the total roughness configuration.

An experiment by Kuester and White [14] looked into the reduction of disturbance energy more closely, and provided more concrete measurements for distributed roughness' effects on stability. They measured a slight delay in transition location in the presence of distributed roughness. Additionally, they measured transient growth in the wake of the distributed roughness, and found that when a discrete roughness element was placed in the field, the total disturbance energy measured was less than the disturbance energy measured behind only the DRE. By decomposing the disturbance energy into different modes based on DRE spacing, they found that the first three modes contained less energy. However, the shorter modes contained more energy due to the increased receptivity of distributed roughness. They used this to suggest that the delay in transition location could not be due solely to a displacement of the boundary layer, but also an interaction of the wakes of the roughness elements.

McMillan et al. [15] performed a follow-up experiment using higher amplitude distributed roughness. The Re_{kk} value of the field (based on the highest peak) was 464, significantly higher than the Downs et al. [12] and Kuester and White [14] experiments. They found that a DRE placed among a distributed roughness field could attain an Re_{kk} of 424 without causing transition, as opposed to the commonly accepted critical value of 334 [4] (when the roughness height to diameter ratio is taken into consideration [16]). This dramatic difference in predicted transition height for the DRE indicates that a strong 'shielding' effect exists, where the presence of small amplitude roughness appears to actually *reduce* the transitional effects of larger amplitude roughness.

1.2 Thesis Objective

The experiments by Kendall [9], Drews [13], Kuester and White [14], and McMillan et al. [15] all demonstrated some consequence of shielding. This counterintuitive effect has rendered even empirical predictors of transition, such as Re_{kk}, unreliable, and highlights researchers' inadequate understanding of distributed roughness effects. Continued experimental and computational efforts, while valuable, are expensive and slow due to the problem's large parameter space. The full parameter space needs further exploration because, as shown in the literature review given above, different types of distributed roughness cause transition via different mechanisms. Developing an analytical model would hopefully capture the effects of distributed roughness and lend some understanding to why roughness fields produce a shielding effect on discrete roughness elements.

An obvious first task for this effort is modeling the base flow using as simple of a method as possible. While DNS methods can produce a base flow for roughness fields, the computational cost is too great to be applied to a significant number of roughness fields. Fortunately, the same experiments which demonstrate the shielding effect also present a possible simplifying process. The experiments by Leventhal and Reshotko [8], Kendall [9], and Tadjfar et al. [10] all present some measurements where a new effective origin was used, shifted away from the original, smooth wall location. By shifting the boundary layer out from the original mean surface, DREs located within the roughness field would have a reduced effect on the mean flow due to their smaller apparent height, as evidenced in the McMillan et al. experiment [15]. This research examines how an 'effective' surface could be used in modeling distributed roughness fields.

The goal of this research is to create a reduced-order, analytical model that describes how laminar boundary layers interact with randomly distributed roughness fields. Several different boundary conditions are examined and paired with different effective surfaces to modify 2D random roughness strips. The different variations of the model presented in this thesis will be evaluated on their performance with regards to three criteria. The model must

1. correctly predict boundary layer quantities above the effective surface, where the highest

peaks in the roughness field remain exposed. The exposed geometry is presumably responsible for eventual transition. Therefore, correctly modeling flow over it is of greater interest in any future transition models.

2. be capable of handling arbitrary, rough, 3D surfaces. Many models only consider wavy walls or similarly small-amplitude, periodic fields that don't resemble real roughness such as that found on a wing.

3. handle the analysis of any roughness patch with significantly less computational cost than a DNS of the same field.

To meet the first goal, the quantitative success of the model is judged solely where the real geometry lies exposed above the effective surface. To evaluate quantitative success, all models will be tested and compared to the true geometry using triple-deck theory, which easily meets the computational cost requirements of the third goal. However, the limitations placed on geometry that is appropriate for triple-deck analysis makes it impossible to fully meet the second goal of handling arbitrarily rough surfaces. The boundary conditions and surfaces are instead considered for their applicability to a 3D scenario. Triple-deck is *not* advocated as an eve

2. MODELING

The main objective of this thesis is to examine the performance of different boundary conditions and effective surfaces for a model of 2D boundary layer flow over distributed roughness. Given a specific configuration, the final model should replicate the 'shielding' phenomenon by reducing the effect of large DREs set among small amplitude distributed roughness. To test the effective surface choices, a large number of random, 2D roughness strips are created and analyzed under numerous effective surface models.

2.1 Parameterization Of Roughness Geometry

Distributed roughness presents a challenging problem partly due to the large parameter space that describes it. It is impossible to predict the exact shape of roughness in a real-world scenario. Therefore this thesis considers the statistical description of the effective surface models' performance over a large number of random roughnesses. Following the method used by Kuester and White, a 2D roughness strip with height distribution $F(x)$ is created using a superposition of cosine waves with randomly generated coefficients [14].

$$F(x) = \frac{h}{\max(\mid F(x) \mid)} \sum_{n=1}^{N-1} A_n \cos(\frac{2\pi n x}{\lambda_{dist}} + \phi_n) \qquad (2.1)$$

The A_n coefficients are generated from a standard normal distribution with a mean of 0 and a standard deviation of 1. The ϕ_n coefficients are selected from a uniformly random distribution between 0 and π. The normalizing factor $h/\max(\mid F(x) \mid)$ is used to control the height of the roughness to test the model on progressively steeper roughness.

The distributed roughness geometry is constrained to remain firmly within the bounds suggested by classical triple-deck theory, which is used to evaluate the models and will be covered in detail in chapter 3. The entire length of the distributed roughness was constrained to be $\mathcal{O}(1)$ and the height limited to $\mathcal{O}(1)$ as well. The number of modes, N, was selected as 3 for this study. A height limit was then enforced to avoid any separation bubbles. To maintain the validity of the

9
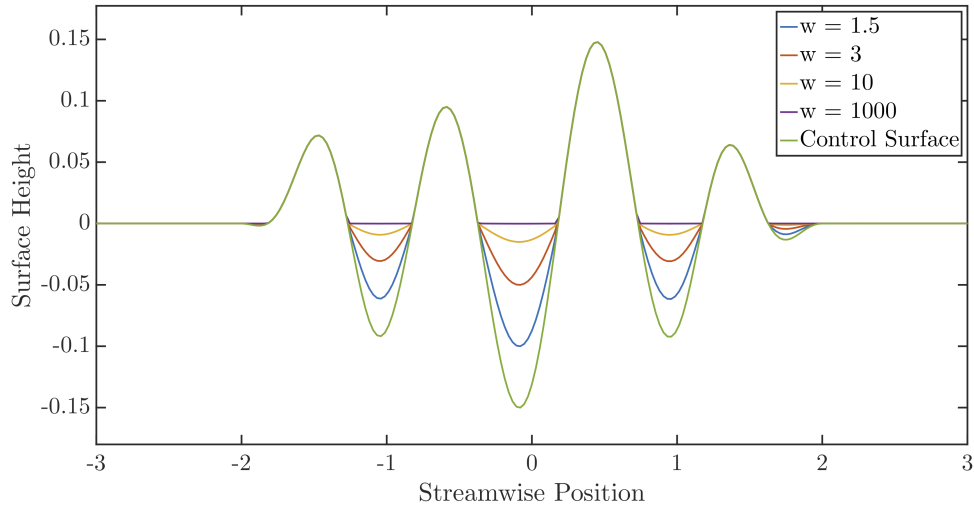
Figure 2.1: Geometry Configurations.

triple-deck equations, it is critical to keep the separation region much smaller than the scale of the roughness. To respect this limit safely, separation was completely avoided.

Admittedly, this 2D, small-scale roughness is far from the coarse roughness of past experiments. However, in the context of the present model, it is useful for evaluating the success of the various effective surfaces and boundary conditions. Future models will need to capture more realistic random roughness.

2.2 Surface Modeling

To create effective surfaces as suggested by the literature (Leventhal and Reshotko [8], Tadjfar et al. [10], Drews [13]) in a simple fashion, the amplitude of the cosine waves that form the real geometry are reduced by a scaling factor (i.e. A_n/w). This gives control over the shape of the effective surface through one parameter w, which allows the effective surface to move between the bounds of matching the real geometry ($w = 1$) and a flat surface at $y = 0$ above any region of negative geometry ($w \to \infty$). A range of configurations are shown in figure 2.1.

This method is easily extensible to 3D roughness formed in the same way (using sines and cosines). Additionally, truly random geometry which is not initially formed using this method can

10

be approximated using a Fourier transform to extract the wavelengths that form the geometry. The more modes used, the better the approximation.

Wherever the true rough surface is exposed, the no-slip boundary condition is applied. Model boundary conditions are imposed where the effective surface is above the real geometry. The three different candidate boundary conditions are considered on the effective surface: no-shear, no-slip, and 'imposed-slip', which are expanded upon below.

2.2.1 No-Shear

The first boundary condition considered is no-shear imposed along the effective surface (denoted as $Y = F^*(x)$).

$$\frac{\partial u}{\partial Y}\Big|_{x,Y=F^*(x)} = 0 \tag{2.2}$$

This is similar to an investigation by Drews using DNS [13] which covered the negative geometry and allowed slip to occur at the new surface. This approach reflects others' experimental observations that negative geometry has much less of an impact on flow that positive geometry. This seems to indicate that the fluid is largely unaffected by geometry below the effective surface, which can be captured best by a no-shear condition. Above the local valleys, the fluid is allowed to accelerate, unhindered by the typical no-slip conditions imposed by real surfaces. This model is easily extensible to 3D roughness, as it is a uniform boundary condition imposed everywhere the effective surface covers the real geometry.

2.2.2 No-Slip

The second boundary condition is a no-slip condition applied at the new effective surface. This choice reflects the observation made by Leventhal and Reshotko that their experimental data could be fit with a Blasius curve, which analytically requires a no-slip condition at the wall [8]. Finding that curve shifted off of the geometric surface suggests that the correct boundary condition for the current model remains as no-slip.

An existing model that examines 2D periodic roughness [17] seems to reinforce no-slip at the effective surface when extrapolated to the limit of very steep, closely packed roughness. This

model, created by Gaster, approximates the flow near sinusoidal roughness as pure Stokes flow, but retains a Blasius boundary layer outer shape. This approach reveals zones of recirculation that produce a raised effective surface. Gaster notes that the recirculation zone is highly dependent on the roughness profiles; as the wavelength of the roughness decreases, the recirculation zone approaches near-zero velocity. He conjectures that this trend would likely continue until sandpaper-like roughness contained zones of static, trapped fluid over which the boundary layer could ride, which is in agreement with what Leventhal and Reshotko observed. This static fluid would therefore act as a no-slip boundary:

$$u(x, Y = F^*(x)) = 0 \tag{2.3}$$

This model is again easily extensible to 3D roughness. However, away from the limit of sandpaper roughness, Gaster's model seems to suggest a different boundary condition where a slip velocity exists at the height of the effective surface, correlated to the geometry of the roughness.

2.2.3 Imposed-Slip

In response to the trends observed in Gaster's model, the following boundary condition of 'imposed-slip' velocity is proposed, offering an intermediate alternative to the no-shear and no-slip boundary conditions. Based on a DNS simulation by Drews [13], it seems important to match the in-plane velocity at the height of the effective surface. In this simulation, which covered the negative geometry with a new surface, a slip velocity was allowed. This slip velocity was very close to the in-plane velocity measured from the control roughness configuration. Comparing disturbance energies downstream showed that the simplified geometry case closely matched the full roughness configuration. Therefore, a method for guessing the velocity at the height of the effective surface is devised.

The first assumption made in creating the slip model is that the effective surface imposes no-penetration, confining the fluid below it. Fluid moving along the effective surface will impart some shear force to that trapped fluid, which influences the confined fluid's recirculation. To model the
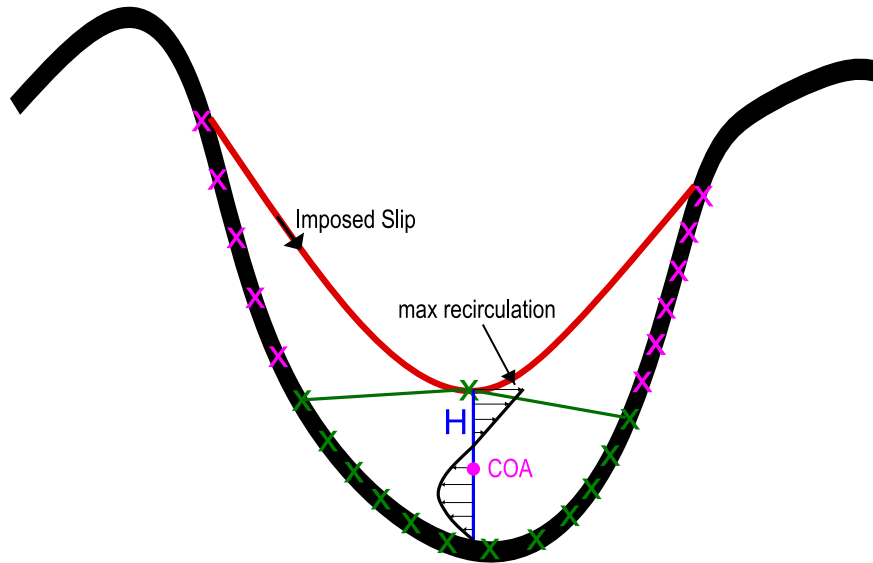
12

Figure 2.2: Some characteristic values used to set the maximum slip velocity.

recirculation motion, the fluid below the surface is considered as a recirculation 'bubble', and related back to Gaster's model. Gaster noted that increasing the height of the roughness caused larger recirculation areas with higher recirculation velocities, while narrower roughness valleys caused slower recirculation velocities. This offers a method of guessing what slip velocity to enforce, based on the geometry of the roughness.

To simplify the recirculation model, only the maximum recirculation velocity is guessed. Once that velocity is modeled and enforced, the velocity along the rest of the surface is linearly ramped back to a no-slip condition at the exposed geometry. Figure 2.2 shows some important geometric values used in defining the maximum recirculation velocity. The black and red surfaces show the real and effective surfaces, respectively. Both are discretized in the computational model, represented by the pink and green crosses along the real surface. The recirculation area is first constrained to a convex, enclosed area (shown outlined in green). This area is defined by identifying the minimum point on the red effective surface, and only considering points on the real surface that fall below that minimum (the green crosses). This exclusion of the upper regions in the recirculation model is justified by assuming that because protruding regions are much narrower than the identified region, they will not produce the maximum recirculation velocity.

13

Next, the center of the green area is calculated (denoted by COA on figure 2.2). The COA specifies the streamwise location of the assumed maximum recirculation velocity. Note that it does not necessarily fall in the same location as the minimum height of the effective surface, although it is usually close. The vertical distance from the real geometry to the effective surface, through the centroid, is defined as H. This variable is intended to reflect how higher roughness causes larger recirculation areas with higher recirculation velocities. A general shape of the recirculation boundary layer was assumed, shown in figure 2.2. To approximate the recirculation velocity at the surface, the top third of the boundary layer was assumed to be linear. A slope of $\lambda_B = 0.332$ was chosen for simplicity.

To account for how narrower roughness valleys cause slower recirculation velocities, the effect of H was offset by considering how the geometry of the green area was distributed. This was calculated by considering the ratio of area moments of inertia about the centroid (I_{yy}/I_{xx}). As the enclosed area becomes more oblong, the ratio adjusts the maximum slip velocity according to Gaster's observations. The resulting final slip velocity formula used for this model is given in equation 2.4.

$$u_{r,max} = \lambda_B (H/3)(I_{yy}/I_{xx})^{1/2}. \tag{2.4}$$

Figure 2.3 shows an example of slip velocities applied to an effective surface. It should be noted that the performance of the model is dependent on the slip velocity prescribed. Here, only one possibility is presented, although further optimization might present a better model. Additionally, the presented recirculation model presents challenges for extension to 3D roughness. The 3D peaks that are exposed will result in spanwise velocity, which would complicate any slip velocity model imposed. However, it should be re-emphasized that the recirculation model is only intended to guess at the velocity at the height of the effective surface. Later, in section 5, it will be determined how much error was introduced by this model, and how this error is correlated to the effective surface model results.
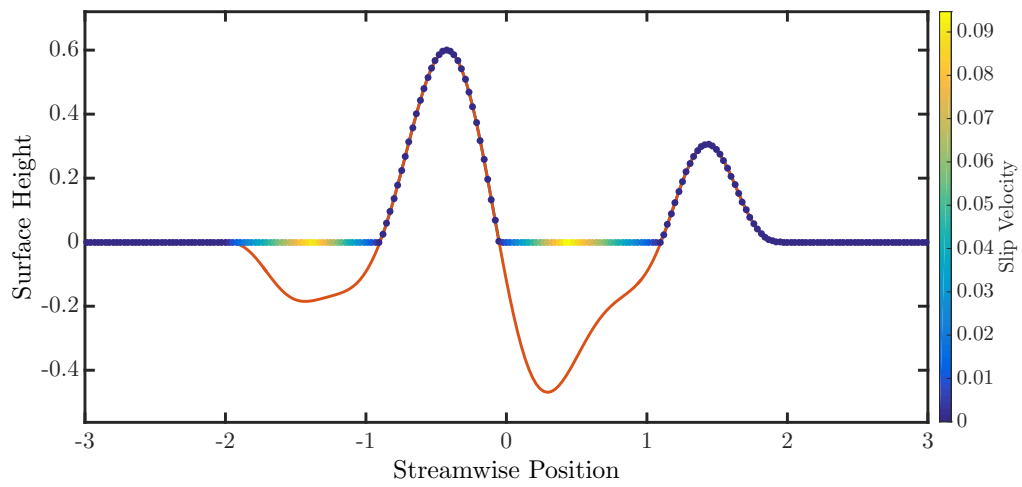
Figure 2.3: Slip velocity applied over smoothed effective surface. Real geometry included for reference on how recirculation geometry affects slip velocity.

3. TRIPLE-DECK THEORY

In order to quantitatively evaluate effective surfaces as a model, the roughness geometry is analyzed using triple-deck theory. This theory was born out of an important research question in the 1960s concerning the upstream influence of downstream features evident in boundary layer experiments. One example of particular concern was the appearance of small separation bubbles upstream of a shockwave in a boundary layer. Boundary layer theory, as well as supersonic inviscid theory, could not cope with this due to the inability of both theories to accommodate upstream influence. Triple-deck asymptotic provided a means of describing this influence by examining a short scaling region that produces a viscous-inviscid interaction.

Triple-deck theory can be derived using the method of matched asymptotic expansions, which considers a Blasius boundary layer as the undisturbed basic state, then mathematically introducing some perturbation. When the Navier-Stokes equations are expanded as an asymptotic series using powers of the Reynolds number, close inspection reveals a set of significant scaling limits. By applying these scalings, three different scaling regimes, or 'decks' emerged. The original derivation was done by Stewartson and Williams [18], Neiland [19] and Messiter [20], who all independently arrived at the correct scalings necessary to describe the viscous-inviscid interaction caused by small disturbances.

Triple-deck interactions (shown in 3.1, where $\epsilon^8 = Re_L^{-1}$) happen on a streamwise length scale of ϵ^3. The decks are vertically scaled as follows: lower deck as ϵ^5, middle deck as ϵ^4, and upper deck as ϵ^3. The lower deck is governed by the incompressible boundary layer equations and is characterized by rotational and viscous disturbances. A passive middle deck exists, still inside the boundary layer, that transmits disturbance information between the upper and lower decks but does not influence the disturbances. The characteristic perturbation in the middle deck is the bending of streamlines, a 'displacement' effect, which is transferred without change to the outer deck. The outer deck, which extends slightly into the freestream, is inviscid and irrotational and is what enables upstream influence. The upper and lower deck are connected through a Hilbert integral

16

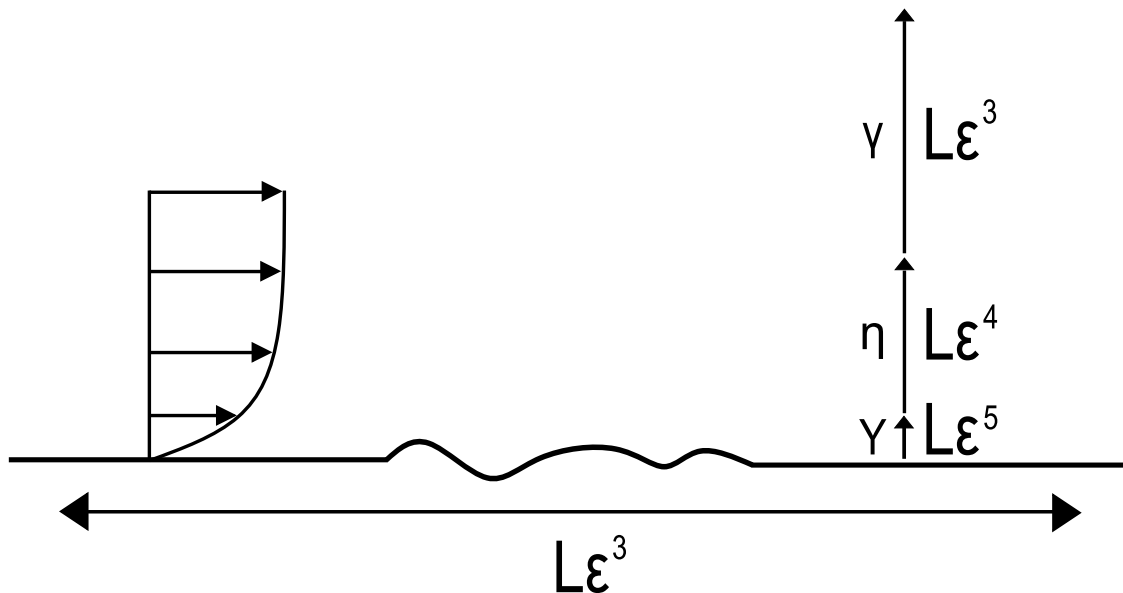which relates displacement and pressure in subsonic flow.

Figure 3.1: Triple-Deck Scalings. $\epsilon^8 = Re_L^{-1}$

Rigorous derivation of the triple-deck scalings requires a thorough examination of what scalings present 'significant' or 'distinguished' limits. To simplify this process, Meyer [21] begins his review of the triple-deck derivation by establishing four guiding physical conditions: 1) mass-flow bound, 2) penetration, 3) localization, and 4) upstream condition. The first condition requires that the displacement thickness remain on the order of $Re_L^{-1/2}$ throughout the length of the interaction. This condition is based upon the experimental observation that small separation bubbles are confined to a thin region of recirculation that does not exceed, in terms of order of magnitude, that of a regular boundary layer. The second condition is captured in Meyer's use of the term 'mild' interaction: strong changes in velocity and pressure that occur in the beginning and ending of separation bubbles requires these disturbances to be felt outside of the viscous region. However, they are not so strong as to completely eliminate the boundary layer structure. The third condition, localization, supposes that the previously mentioned changes occur over a region that shrinks to a point when examining the entire body (i.e. as the vehicle-scale Reynolds number becomes very

large). Finally, the upstream condition indicates that, at some large distance upstream of these disturbances, the boundary layer will not be affected by the downstream disturbance and will be a classical Blasius boundary layer.

Triple-deck theory provides a number of physical insights surrounding small separation bubbles. This 'mild' interaction between the viscous boundary layer and the inviscid outer deck can not be mathematically captured by an inviscidly determined pressure gradient applied to Prandtl's boundary layer equations. Computational evidence of this fact resulted in what was termed 'Goldstein's singularity', where upon approaching a separation bubble the computational solution would blow up [22]. On scales relevant to triple-deck there exists what Veldman termed a 'loss of hierarchy', where neither the pressure gradient nor a viscous displacement term is able to singularly determine the flow [23]. Instead, both variables are necessary for a unique solution, 'communicating' through the decks and through an interaction principal. For subsonic flow, the elliptic outer deck provides an upstream route that allows information to travel upstream.

Motivation for applying this theory stems from the desire to explore the physical mechanisms in distributed roughness while maintaining computational inexpensiveness. Triple-deck theory not only provides an inexpensive method for allowing upstream influence, but also neatly resolves small separation bubbles that arise between the roughness elements. Additionally, the use of the boundary layer equations allows the use of Prandtl's transposition theorem [24], which transforms the random roughness into a rectangular computational grid, further lessening computational complexity.

A limiting factor in the use of triple-deck theory is the scale of the roughness field being examined. Violating the scalings used in the derivation of the triple-deck equations could imply that previously neglected terms may be becoming leading order. Rothmayer and Smith provide a thorough review of the different hump scalings and the resulting simplified equations [25]. Extensive analysis, however, has shown some overlap with nearby scalings. Smith et al. examined some discrepancies between past reviews of different hump scalings [26]. They showed that although triple-deck is derived in a very specific scaling region, it provides a correct, first-order analysis over

similar scaling regions. On scales longer than triple-deck but at a similar height, the bump does not provoke separation but merely displaces the boundary layer. On shorter scales, as the length of the bump decreases so too does the critical height that first provokes separations. Smith et al. shows how triple-deck theory is a leading order or limiting solution for the more precisely scaled solution for the shorter and longer humps, so long as the non-linear regions above the critical height are avoided.

Not only does the critical height change, the driving feature of the flow changes as well [23]. On scales longer than triple-deck lengths the flow is driven by a pressure gradient, as in classical boundary layer theory. On shorter scales the flow is driven by the displacement term. The non-hierarchal approach of triple-deck allows the theory to approach the neighboring scalings without difficulty.

Further exploration of triple-deck theory has shown its usefulness in applications that seem far away from its intended limits. Tsao and Rothmayer use triple-deck theory to examine ice accumulation on airfoil surfaces, which allows for distributed roughness like surfaces to form [27]. In light of the above evidence, triple-deck theory has been used in this exploratory study to examine different boundary conditions and effective surface heights. To respect the scaling criteria, a distributed roughness strip that meets the scaling guidelines will be used. The method of this strip's creation is covered in chapter 2.

The following sections will present the full triple-deck equations. This thesis will not attempt to prove *a priori* that any assumptions made and scalings assumed are correct. It will simply show the scalings used to derive the triple-deck structure, and highlight some important physical and mathematical aspects of the resulting equations. The full derivation for this problem was originally done by Stewartson and Williams for supersonic flow [18]. Here, the equations are restricted to 2D subsonic flow.

Triple-deck theory makes an asymptotic approximation to the Navier-Stokes equations by assuming $Re \to \infty$, or $\epsilon \to 0$. Appropriate scaling choices will reveal which terms are leading order and which may be neglected in this limit. Each deck will use the non-dimensionalized variables

given in equation 3.1 (a^* denotes a dimensional variable, a_∞ denotes a freestream value). Due to the assumptions of incompressibility and constant temperature, ρ and μ are both set equal to unity.

$$u = \frac{u^*}{U_\infty} \qquad v = \frac{v^*}{U_\infty} \qquad p = \frac{p^* - p_0^*}{\rho_\infty U_\infty^2} \qquad \rho = \frac{\rho^*}{\rho_\infty} \qquad \mu = \frac{\mu^*}{\mu_\infty} \qquad (3.1)$$

The streamwise length scale remains the same throughout the decks: $X = \epsilon^{-3} x^*/L$. Note that this scaling leads to X being an $\mathcal{O}(1)$ variable. This will be true for all non-dimensionalized flow and geometry variables; the ϵ terms will determine leading-order terms.

3.1   Middle Deck

Beginning with the middle deck, the normal variable will scale as $\eta = \epsilon^{-4} y^*/L$, the same scaling as a Blasius boundary layer. Recall a physical assumption used is that even in the case of small separation bubbles, the region of recirculation is confined to a small area and does not cause a large change in boundary layer size. Assume that a disturbance (such as a roughness field) creates a perturbation in the flow. Assuming some prior knowledge of the correct form of the equations, the flow variables can be expanded in terms of ϵ to the series shown in 3.2 - 3.4.

$$u = U_B(\eta) + \epsilon u_1(X, \eta) + \epsilon^2 u_2(X, \eta) + ... \qquad (3.2)$$

$$v = \epsilon^2 v_1(X, \eta) + \epsilon^3 v_2(X, \eta) + ... \qquad (3.3)$$

$$p = \epsilon^2 p_1(X, \eta) + \epsilon^3 p_2(X, \eta) + ... \qquad (3.4)$$

Here, U_B refers to the base flow, a Blasius flow, with all other terms being the perturbations to that flow. Substituting these terms into continuity along with the scaling for X and η yields the following:

$$\frac{\partial u_1}{\partial X} + \epsilon \frac{\partial u_2}{\partial X} + \frac{\partial v_1}{\partial \eta} + \epsilon \frac{\partial v_2}{\partial \eta} = 0 \qquad (3.5)$$

Considering the limit of $\epsilon \to 0$, the first and third terms remain as leading-order terms, tending to zero at the same rate as 1 (i.e. $\mathcal{O}(1)$) while the second and fourth terms going to zero at the rate of ϵ (i.e. $\mathcal{O}(\epsilon)$). Classical triple-deck theory is a first-order approximation and therefore neglets any

higher-order terms. The analysis here shall only retain first-order terms as well.

Repeating the same procedure for the x and y-momentum equations (and additionally substituting $Re_{\infty,L} = \epsilon^{-8}$) reveals the governing equations for the middle deck:

$$U_B \frac{\partial u_1}{\partial X} + v_1 \frac{\partial U_B}{\partial \eta} = 0 \tag{3.6}$$

$$\frac{\partial p_1}{\partial \eta} = 0 \tag{3.7}$$

Equation 3.6 is locally inviscid even within the boundary layer. No viscous terms remain significant in this approximation. This already indicates the need for an inner deck. Equation 3.7 indicates that the disturbance caused by the lower deck is not transmitted through a vertical pressure gradient. The middle deck solution, equations 3.8 and 3.9, allows for a different variable to be responsible for moving the disturbance out of the boundary layer.

$$u_1 = A_1(X)U_B'(\eta) \tag{3.8}$$

$$v_1 = -U_B(\eta)A_1'(X) \tag{3.9}$$

It was mentioned above that the primary feature of the middle deck was the passive transfer of information. This is shown here in the perturbation terms as $A_1(X)$ (hereafter refered to as the displacement term, representing $-\delta(x)$). The displacement term is related to how streamlines are bent as they move around an obstacle. The middle deck has no influence on this value (shown by A's sole dependence on X), which allows computational analysis of triple-deck theory to concern itself only with the lower and upper decks.

The upstream boundary conditions are satisfied by requiring the displacement term to go to zero. It is assumed to not be identically zero in the region of interest (this would not present a significant scaling limit). However, these equations cannot satisfy boundary conditions at $\eta \to \infty$ or at $\eta \to 0$, therefore additional decks are required to intervene with new scales.

3.2 Lower Deck

The lower deck intervenes below the middle deck to satisfy the no-slip condition as $\eta \to 0$. The normal variable is scaled as $\tilde{Y} = \epsilon^{-5}y^*/L$. In this region, the perturbation is no longer small compared to the base flow, which is assumed to be linear in the region close to the wall. The following scaling is required to allow for a balance between the non-linear transport terms and the friction forces:

$$u = \epsilon U(X, \tilde{Y}) + \epsilon^2 \tilde{u}_2(X, \tilde{Y}) + ... \tag{3.10}$$

$$v = \epsilon^3 V(X, \tilde{Y}) + \epsilon^4 \tilde{v}_2(X, \tilde{Y}) + ... \tag{3.11}$$

$$p = \epsilon^2 P(X, \tilde{Y}) + \epsilon^3 \tilde{p}_3(X, \tilde{Y}) + ... \tag{3.12}$$

After substitution into the Navier-Stokes equations, the lower deck governing equations are revealed to be the boundary layer equations.

$$\frac{\partial U}{\partial X} + \frac{\partial V}{\partial \tilde{Y}} = 0 \tag{3.13}$$

$$U\frac{\partial U}{\partial X} + V\frac{\partial U}{\partial \tilde{Y}} = -P'(X) + \frac{\partial^2 U}{\partial \tilde{Y}^2} \tag{3.14}$$

$$\frac{\partial P}{\partial \tilde{Y}} = 0 \tag{3.15}$$

All wall boundary conditions can be satisfied at this point. Equations 3.16 - 3.18 represents no slip and no penetration, matching with upstream flow, and matching with middle deck, respectively.

$$U = V = 0 \quad \text{on} \quad \tilde{Y} = hF(X) \tag{3.16}$$

$$\frac{\partial U}{\partial \tilde{Y}} \to 1 \quad \text{as} \quad X \to -\infty \tag{3.17}$$

$$U \to \lambda(\tilde{Y} + \tilde{A}(X)) \quad \text{as} \quad \tilde{Y} \to \infty \tag{3.18}$$

However, the pressure gradient cannot be set *a priori*, or the Goldstein singularity will appear in a computational solution. The outer deck, which has yet to be determined, will connect the pressure gradient in the lower deck with the displacement transmitted through the decks.

3.3 Upper Deck

The upper deck, scaled as $\gamma = \epsilon^{-3}y^*/L$, extends up into the inviscid region. The expansions chosen here are perturbations to the freestream flow ($u = U_\infty = 1$):

$$u = 1 + \epsilon^2 U_2(X, \gamma) + \dots \tag{3.19}$$

$$v = \epsilon^2 V_2(X, \gamma) + \dots \tag{3.20}$$

$$p = \epsilon^2 P_2(X, \gamma) + \dots \tag{3.21}$$

After substitution, the upper deck governing equations are revealed to be inviscid, irrotational equations, as expected.

$$\frac{\partial U_2}{\partial X} = -\frac{\partial v}{\partial \gamma} \tag{3.22}$$

$$\frac{\partial U_2}{\partial X} = -\frac{\partial p}{\partial X} \tag{3.23}$$

$$\frac{\partial V_2}{\partial X} = -\frac{\partial p}{\partial \gamma} \tag{3.24}$$

The solution to these equations that correctly matches with the other decks can be found using complex analysis.

$$P'(x) = \frac{-1}{\pi} \int_{-\infty}^{\infty} \frac{A''(\xi)d\xi}{x - \xi} \tag{3.25}$$

The integral in equation 3.25 is a Hilbert Integral, where the integral is taken as the Cauchy Principal Value integral, denoted with a slash through the integral sign.

The above description closes the mathematical description of a triple-deck interaction. The

necessary equations for computationally simulating this interaction are contained below:

$$u_X + \tilde{v}_{\tilde{Y}} = 0, \tag{3.26}$$

$$uu_X + \tilde{v}u_{\tilde{Y}} = -p_X + u_{\tilde{Y}\tilde{Y}}, \tag{3.27}$$

$$p = -\frac{1}{\pi} \int_{-\infty}^{\infty} \frac{\tilde{A}'(\xi)d\xi}{\xi - X}, \tag{3.28}$$

$$u(X, \tilde{y} = hF(X)) = 0, \tag{3.29}$$

$$u \to \lambda\tilde{Y} \quad \text{as} \quad X \to -\infty, \tag{3.30}$$

$$u \to \lambda(\tilde{Y} + \tilde{A}(X)) \quad \text{as} \quad \tilde{Y} \to \infty \tag{3.31}$$

4. COMPUTATIONAL METHODS

To simulate the triple-deck equations, the quasi-simultaneous method of Veldman is used [28]. The boundary layer equations (3.26 - 3.27) are coupled with the interaction equation (3.28) and solved simultaneously at each streamwise node. Before solving these equations, the Prandtl transposition (4.1) [24] is applied to transform the random physical domain to a rectangular computational domain. Variables with a $\sim$ are untransformed variables.

$$\tilde{Y} = Y + h, \qquad \tilde{A} = A - h, \qquad \tilde{v} = v + uh_x \tag{4.1}$$

A is defined as the negative displacement variable, and h is the height of the geometry above the mean surface. The boundary layer equations are unchanged by this transformation. The interaction law and boundary conditions change to:

$$p(x) = \frac{1}{\pi} \int_{\infty}^{\infty} \frac{h'(\xi) - A'(\xi)}{\xi - x} d\xi, \tag{4.2}$$

$$u(x, Y = 0) = 0, \tag{4.3}$$

$$u \to \lambda Y \qquad \text{as} \qquad x \to -\infty, \tag{4.4}$$

$$u \to \lambda(Y + A) \qquad \text{as} \qquad Y \to \infty \tag{4.5}$$

To cluster points near the wall around the roughness, the Y coordinate is transformed into the η space using $\eta = Y/(1 + Y)$. The computational domain is evenly divided into a cartesian grid. Figure 4.1 shows the grid nomenclature and spacing along with the expansion location for the discretized equations. The blue dot corresponds to the x-momentum equation. The red dot corresponds to the continuity equation. The green dot corresponds to the interaction equation.

To solve the boundary layer equations, the streamwise velocity is split into two components: the base shear flow, λY, and the perturbation quantity, $\hat{u}$. X-momentum is discretized using finite
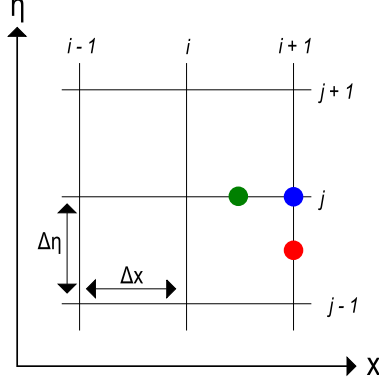
Figure 4.1: Grid Nomenclature

difference representations expanded about the grid point $(i + 1, j)$, shown in equations 4.6 - 4.8.

$$\frac{\partial a}{\partial x} = \frac{3a_{i+1} - 4a_i + a_{i-1}}{2\Delta x}, \tag{4.6}$$

$$\frac{\partial a}{\partial \eta} = \frac{a_{j+1} - a_{j-1}}{2\Delta \eta}, \tag{4.7}$$

$$\frac{\partial^2 a}{\partial \eta^2} = \frac{a_{j+1} - 2a_j + a_{j-1}}{\Delta \eta^2} \tag{4.8}$$

Note that the three-point backwards stencil for $\partial/\partial x$, while unusual for implicit schemes expanded about $(i + 1, j)$, is necessary to prevent oscillations [29]. The convection terms required linearization, which is performed using Newton's method. Local iterations at each streamwise node are necessary to converge the lagged variables. This generally takes 2-3 iterations. Continuity is expanded about $(i + 1, j - 0.5)$, and is differenced as shown below:

$$\frac{3u_{i+1,j} - 4u_{i,j} + u_{i-1,j} - 3u_{i+1,j-1} + 4u_{i,j-1} - u_{i-1,j-1}}{4\Delta x} + \frac{v_{i+1,j} - v_{i+1,j-1}}{\Delta \eta} = 0 \tag{4.9}$$

The boundary layer equations are required to be solved in a coupled fashion to reduce oscillations [29]. In addition, proper treatment of the loss of hierarchy between the lower deck and upper deck requires the boundary layer equations be solved simultaneously with the interaction law. Extensive treatment of this point is given by Veldman [23].

The discretization of the interaction law follows the example laid out by Sychev [30] (first

26

proposed by Veldman [28]). First, the infinite bounds of the integral are exchanged for the finite bounds of the computational domain. Convergence studies showed little effect to extending the range of the computational domain. Next, the interaction law is expanded at $(i + 0.5)$, shown in equation 4.10. Note the constant vertical pressure gradient allows the same equation to be applied at all vertical nodes on a single streamwise node.

$$p(x_i) = \frac{1}{\pi} \sum_{j=1}^{N-1} \frac{h'_{j+0.5} - A'_{j+0.5}}{\xi_{j+0.5} - x_{j+0.5}} \Delta\xi \tag{4.10}$$

The derivatives h' and A' are discretized (again to second order) about the point $(i + 0.5)$ as follows:

$$\frac{\partial a}{\partial x} = \frac{a_{i+1} - a_i}{\Delta x} \tag{4.11}$$

Equation 4.10 is rewritten to be only in terms of variables at the $(i+1)$ station. The substitution $\alpha_{ij} = 1/(\pi\Delta x((i - j)^2 - 0.25))$ is used, along with the outer boundary condition (eqn. 4.5) to replace A_{i+1}^{n+1} with $u_{i+1,nY}/\lambda$.

$$p_{i+1}^{n+1} - \alpha_{i+1,i+1}(h_{i+1} - \frac{u_{i+1,nY}}{\lambda}) = \sum_{j=2}^{i} \alpha_{i+1,j}(h_j - A_j^{n+1}) + \sum_{j=i+2}^{N-1} \alpha_{i+1,j}(h_j - A_j^n) \tag{4.12}$$

Upstream of the $(i + 1)$ station (the first summation), pressure and displacement terms are used from the current iteration, while downstream (the second summation), the terms come from the previous iteration.

Equation 4.12 is substituted into x-momentum and coupled with continuity. The equations form a system of $2nY$ equations with $2nY$ unknowns. The matrix, M, is nearly banded with a band width of 6 and an additional half-full last column resulting from the substitution of the interaction equation into x-momentum (the $u_{i+1,nY}$ term). To solve this in a computationally efficient manner, the Sherman-Morrison algorithm is used [31].

Two new vectors, u and v, are selected such that $M = (A+u\otimes v)$, where A is a banded matrix. Here, u consists of the pressure terms and v is a unit vector e_j, where $j = 2nY - 1$. After solving
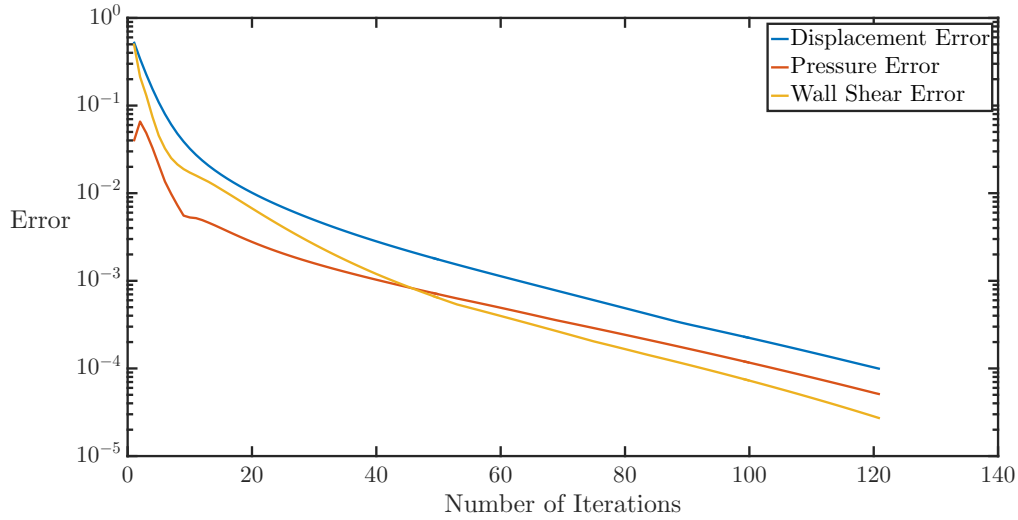
Figure 4.2: Error Convergence

$Ay = b$ and $Az = u$, the final solution simplifies to:

$$x = y - \left(\frac{y_j}{1 + z_j}\right)z \tag{4.13}$$

Beginning far upstream, a Blasius solution is assumed ($\hat{u} = 0$ everywhere). Marching downstream, the above algorithm is invoked at every streamwise station, iterating to properly converge the linearized terms. Once the solution falls below a specific convergence criteria (error $< 10^{-5}$), the solution proceeds to the next streamwise node. Since all downstream nodes use pressure and displacement values from the previous iteration, global iterations are required. Due to the quasi-simultaneous nature of this scheme, the global iteration are over-relaxed according to equation 4.14, using $\omega = 1.5$.

$$A(n + 1) = (1 - \omega)A(n) + \omega A(n + 1) \tag{4.14}$$

The solution was assumed to be converged when the displacement error fell below 10^{-4}. Figure 4.2 shows how the error of the displacement, pressure, and wall shear stress changed.

Several studies were performed to ensure the solutions were properly converged. The ones shown below were performed while analyzing the geometry from Smith [32]. The step size studies
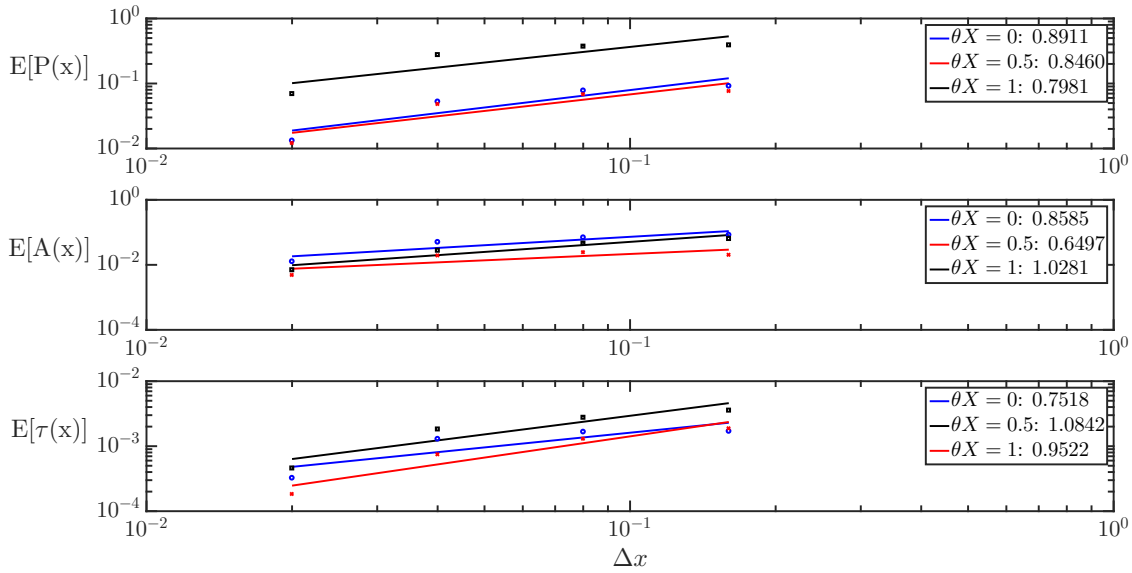
28

Figure 4.3: X Step Size Study

are shown in figures 4.3 and 4.4. The values displayed in the legend indicate the slope of the fitted

line on a log-log scale.

It is interesting to note that, despite consistent second-order differencing, all global variables

show first-order convergence behavior in x. One possible explanation for this is the peculiar dif-

ferencing scheme required to evaluate the Cauchy integral for the interaction law. No further

investigation of this point was made. The step study in η performed slightly better than first-order

behavior.

A few studies were performed to select the domain bounds. While holding step size constant,

the x domain was expanded from 30 to 60 in increments of 10. When comparing relative error

between the domain changes, the largest effect was seen in the pressure variable. However, the

change between the two smallest domains was less than a percent. Changing between domain

sizes of 50 to 60 resulted in 0.1% change in pressure. The changes in displacement and shear

stress were negligible compared to this. Changing η bounds had a similar result. Shear stress

changes were negligible, however displacement and pressure errors did not fall below 1% until the

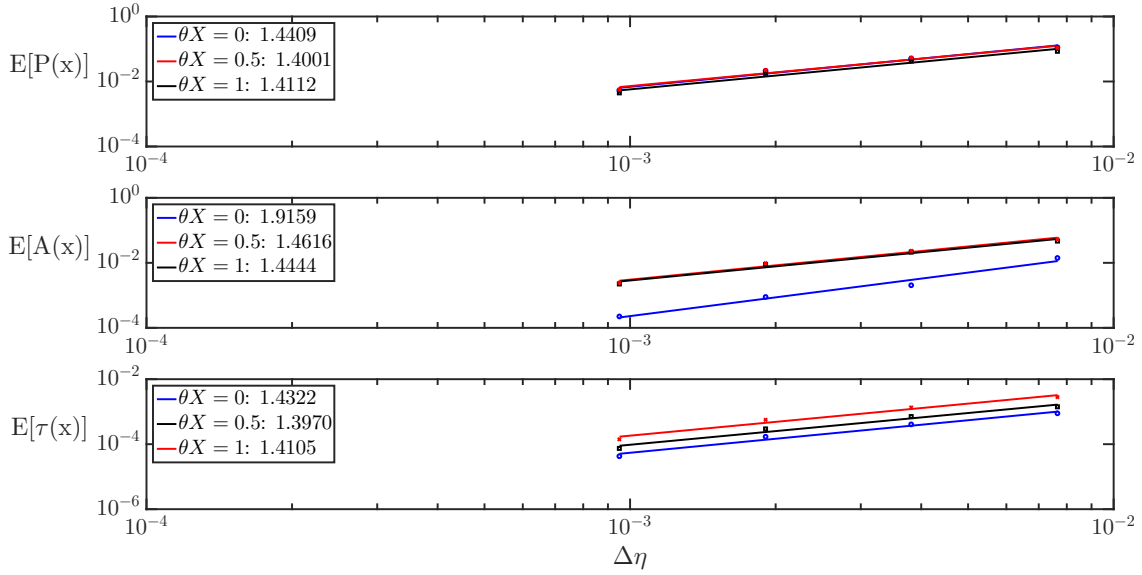η bound was moved to the max value of 0.98.

Figure 4.4: η Step Size Study

Final parameters selected to examine the roughness were:

Parameter	Value
x Domain Size	40
η Domain Size	0.95
nX	1501
nY	500

To verify the current code produces the correct solution, it was compared against two canonical roughness cases. As a note on the comparisons to be shown, most historical literature made a simplification by taking $\lambda = 1$. To correctly compare between the two codes, the following transformations must be put in place for geometry and output variables [33]. A variable such as $\hat{x}$ has been transformed such that $\lambda = 1$.

$$x = \lambda^{-5/4}\hat{x}, \qquad y = \lambda^{-3/4}\hat{y}, \qquad u = \lambda^{1/4}\hat{u}, \tag{4.15}$$

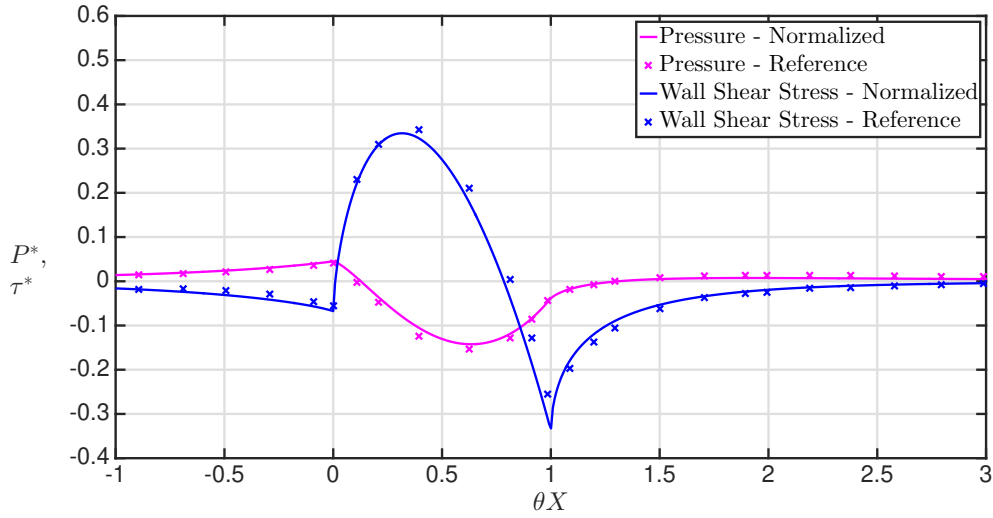$$v = \lambda^{3/4}\hat{v}, \qquad A = \lambda^{-3/4}\hat{A}, \qquad p = \lambda^{1/2}\hat{p} \tag{4.16}$$

Figure 4.5: Code Validation for linear hump. $h = 0.1$. The values shown are normalized. Assuming $\lambda = 1$, $P^* = p/h$, $\tau^* = (\tau_w - 1)/h$. Reference data is from Napolitano and Werle [2]

The first case is the linear bump first examined analytically by Smith in 1973 [32], and later numerically by Napolitano and Werle [2]. Its geometry is given by equation 4.17, where $\theta = 0.8272$.

$$\hat{h}F(\hat{x}) = \hat{h}\frac{\hat{x}(1 - \theta\hat{x})}{\theta} \tag{4.17}$$

Shown in figure 4.5 is a comparison between data taken from Napolitano and Werle and data produced by the current code. The comparison between the two codes is convincing.

To further test the code, the quartic hump studied by Sykes [34] was analyzed. The geometry is given by:

$$\hat{h}F(\hat{x}) = \hat{h}(1 - \hat{x}^2)^2 \tag{4.18}$$

Using a value of 3 for $\hat{h}$ guarantees a separation bubble on the leeward side of the bump. Shown in figure 4.6 is the comparison between between the two codes.

There is a small discrepancy in the shear stress values in the area of recirculation. This can be explained by the difference in models used in those areas. Sykes used an approximation known as FLARE, where $u\partial u/\partial x$ is set to zero in the interest of numerical stability [35]. The same
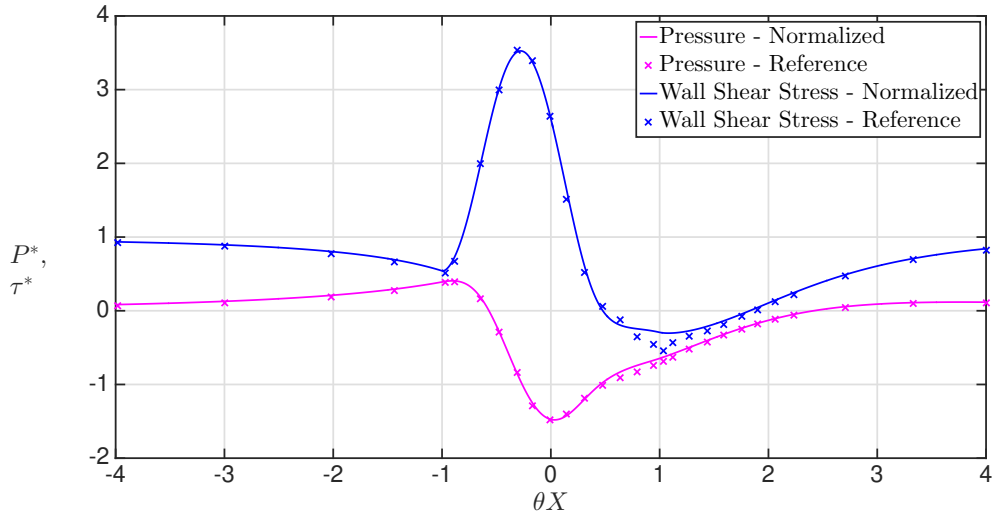
31

Figure 4.6: Code Validation for quartic hump. $h = 0.1$. The values shown are normalized. Assuming $\lambda = 1$, $P^* = p/h$, $\tau^* = (\tau_w - 1)/h$.

approximation in the current code resulted in severe oscillations where there should have been a smooth separation bubble. Veldman also noted the lack of use of FLARE in his paper [28].

The two cases shown are considered proof that the current code gives reliable results for geometry within the scope of triple-deck theory.

5. RESULTS

The primary concern of this thesis is matching shear stress results over exposed geometry using an 'effective surface' model. Here, the model consists of reducing the depth of negative geometry, and coupling the new surface with a trial boundary condition to offset the change. To evaluate how well the modeled effective surfaces match control geometry, several parameters are examined. First, the RMS error is computed using equation 5.1, where τ_R refers to shear stress computed for the control geometry, and τ_M refers to shear stress computed for the modeled geometry and effective surface combination.

$$E_{RMS} = \sqrt{\frac{\sum_{i=1}^{N}(\tau_R(x) - \tau_M(x))^2}{N}} \tag{5.1}$$

RMS error quantifies the average difference between the modeled shear stress and the control shear stress. This parameter captures both undershoot and overshoot errors. To separate the influence of the two types of error, the RMS overshoot error is calculated using equation 5.2.

$$O_{RMS} = \sqrt{\frac{\sum_{i=1}^{N}(\max(\tau_M(x) - \tau_R(x), 0))^2}{N}} \tag{5.2}$$

Overshoot error is indicative of modeled geometry being more severe than in reality; this may lead to falsely indicating transition would occur. Finally, the maximum overshoot magnitude and location is computed, for similar reasons.

All calculations are only performed where the real geometry lies exposed over the effective surface. This is done because a stability analysis would be adversely affected by the largest elements, which are likely to cause transition. All calculations are normalized by the range of shear stress measured over the exposed control geometry. This enables comparisons on overall model performance between different geometry heights.

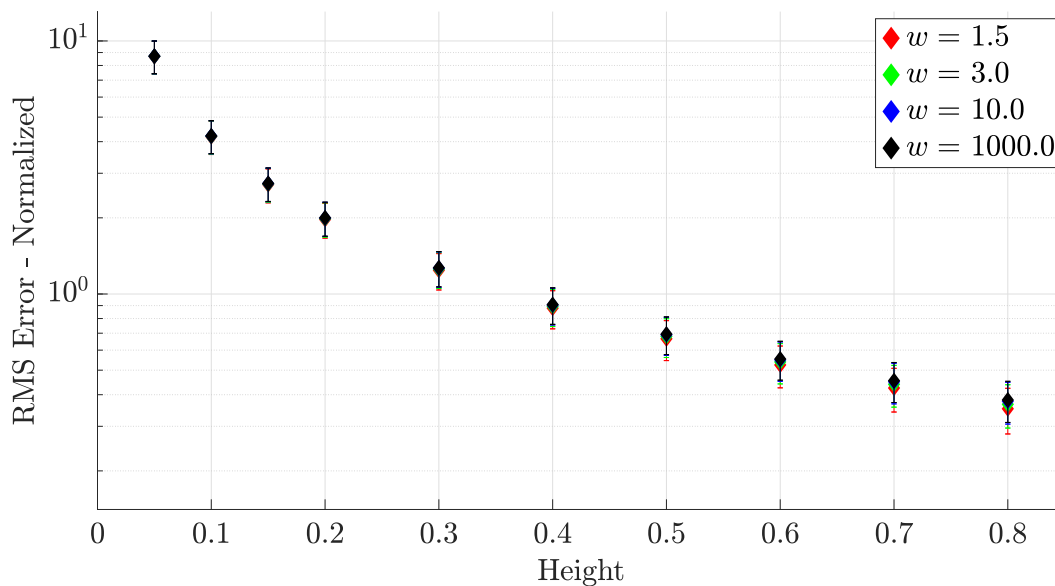A total of 100 random geometries are created for analysis. For each geometry, four effective

Figure 5.1: RMS error for no-shear (normalized by the range of shear stress measured in the control configuration)

surface heights are tested, with ω (smoothing) values of 1.5, 3, 10, and 1000. An example of the difference between the effective surfaces is shown in figure 2.1. Each effective surface is tested using the three different boundary conditions. The mean values for RMS error and overshoot, along with the mean maximum overshoot, are presented for the same group of 100 geometries.

5.1 No-Shear Effective Surface Boundary Conditions

The following results examine geometries where no-shear is applied at the effective surface. The relative RMS error produced by no-shear is up to two orders of magnitude larger than the error produced by any other modeled configuration. However, the spread in these results is relatively small; standard deviations are roughly $15 - 20\%$ of the mean error. Figure 5.1 shows how the normalized mean RMS error changes as the height of the roughness increases. As the geometries become taller, the relative error produced by a specific effective surface decreases. Improvement in relative error (shown as solid lines in figure 5.2), is at first large ($\sim 70\%$ as h climbs in increments of 0.1). However, this improvement gradually slows down to roughly 18%.

Unnormalized values (shown as dashed lines in figure 5.2) reveal most of the improvement
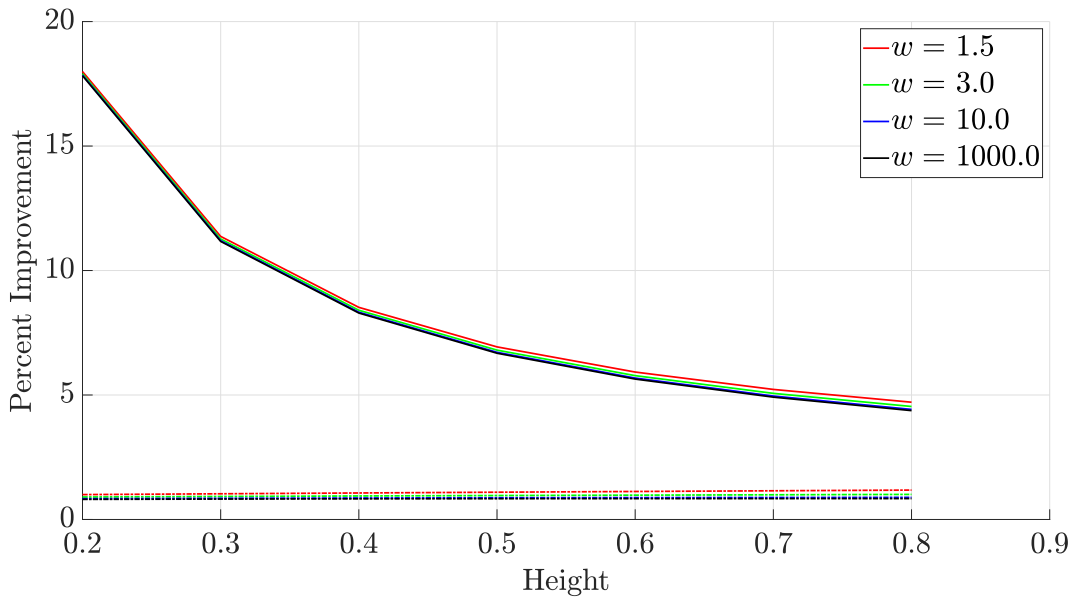
Figure 5.2: Percent improvement in RMS error for no-shear, effective surface height held constant. Solid lines are normalized, dashed lines are unnormalized.

in error stems from the increase in the range of the shear stress values. Removing this effect shows improvement is steady at $\sim 1\%$. All trends are similar regardless of effective surface height, although the difference in value increases as the height of the geometry increases. When comparing results between effective surfaces at the same geometry height, the difference between the two bounding surfaces ($\omega = 1.5$ and 1000) is very small at first (0.3%) but increases to 8% for the steepest roughness. Relative to the other boundary conditions, this is still very small. All of the error produced by the no-shear model is overshoot error (a representative example is show in figure 5.4). Figure 5.3 shows the RMS overshoot, which matches the total RMS error. No further O_{RMS} figures will be shown.

Trends are similar for maximum overshoot. The maximum overshoot always occurs at the first node located on the exposed geometry. This is due to the sudden switch from no-shear back to no-slip, when the velocity at the wall has increased over the effective surface. The fluid near the wall is suddenly stopped, which causes a streamwise and normal gradient. As the geometries become taller, the maximum overshoot decreases (shown in figure 5.5). Figure 5.6 shows the improvement
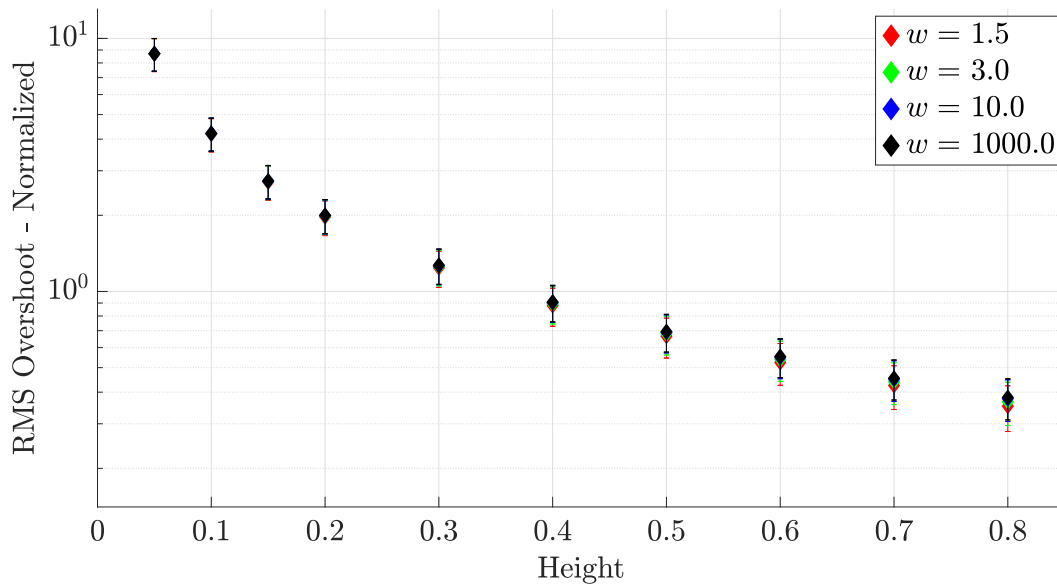
Figure 5.3: RMS overshoot for no-shear (normalized by the range of shear stress measured in the control configuration)
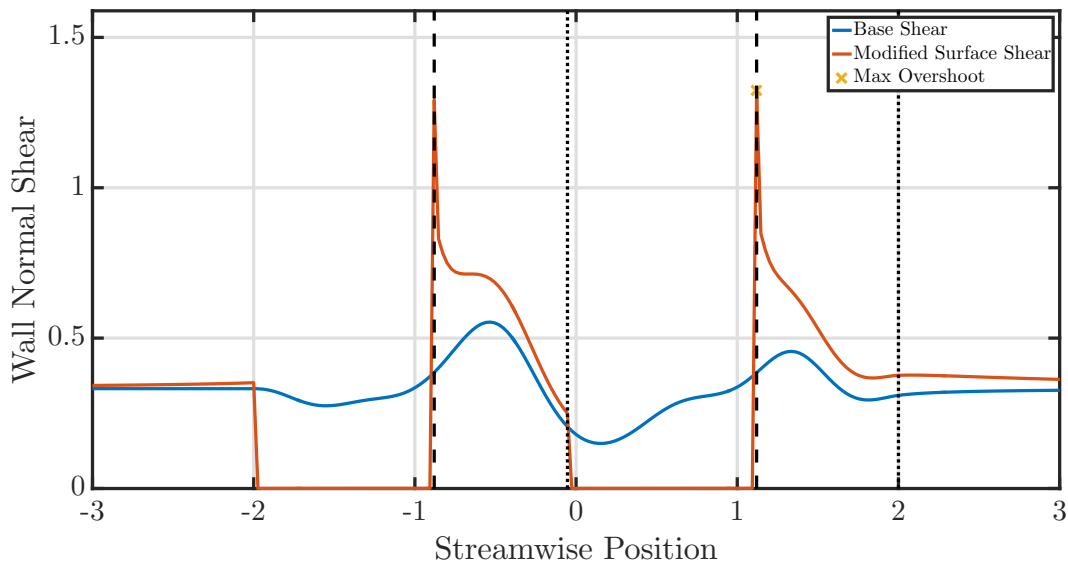

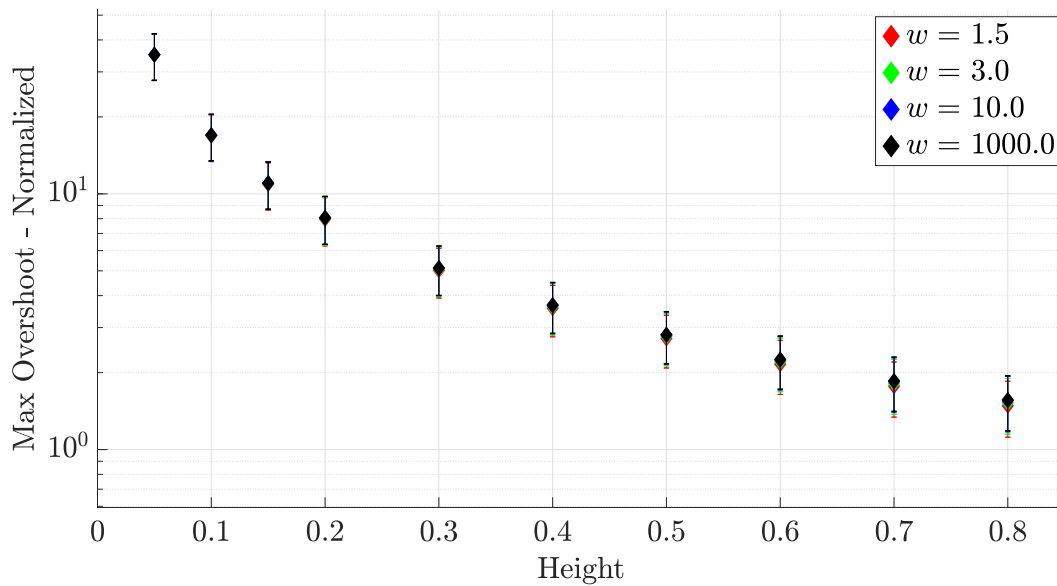Figure 5.4: Example of no-shear results.

Figure 5.5: Maximum overshoot for no-shear (normalized by the range of shear stress measured in the control configuration)

in maximum overshoot as the height increases. The improvement is smaller as the roughness becomes steeper. As mentioned before, this was partly due to the fact that the range in shear stress increased. Neglecting this change in base shear stress showed the maximum overshoot decreased $\sim 1\%$. The similarity between these results and the E_{RMS} results is due to the large effect outliers have on calculating an RMS value.

The improvement in maximum overshoot as heights increase is somewhat puzzling at first. However, triple-deck theory over a standard bump on a flat plate reveals a dip in shear stress prior to the start of the hump. The larger the bump, the more extreme this reduction in gradient can be, sometimes leading to separation in front of the bump. Hence, as the geometry increases, the shear stress would fall more dramatically in front of the bump. This standard dip in shear stress is masked here partly because the geometry is continuous amidst the distributed roughness strip. It is also partly masked by the large spike caused by the return to the no-slip condition.

The large spike in shear stress that is persistent in this model results in a poor match with the control, although the model is consistent regardless of effective surface height.
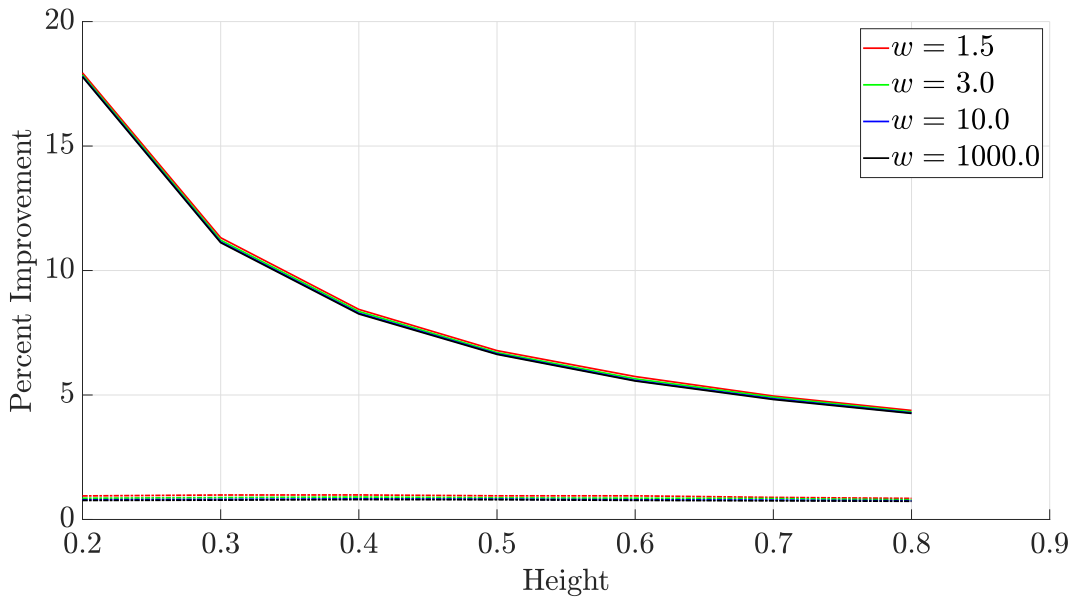
Figure 5.6: Percent improvement in maximum overshoot for no-shear, effective surface height held constant. Solid lines are normalized, dashed lines are unnormalized.

5.2 No-Slip Effective Surface Boundary Conditions

The following results examine geometries where no-slip was applied at the effective surface. No-slip never overestimates shear stress for any modeled geometry. A representative example of no-slip applied to a distributed roughness patch is shown in figure 5.7. Therefore, only the RMS error will be presented here. Figure 5.8 shows how the normalized error decreases as the height of the geometry increases. No-slip is also fairly consistent in its results; standard deviation is roughly $18 - 20\%$ of the mean E_{RMS}. However, there is a large difference in results when comparing between different effective surface heights.

The percent difference in RMS error between the bounding effective surfaces is extreme for the no-slip case ($\sim 99\% - 109\%$). This large dependence on effective surface height is unsurprising; without changing the boundary condition, the change in height cannot be offset. The increase in percent difference as the height of the geometry is increased is explained by the effective surface methodology. By using ω as a smoothing factor, only the relative difference in effective surface heights is constant. As the roughness gets steeper, the absolute difference between the effective
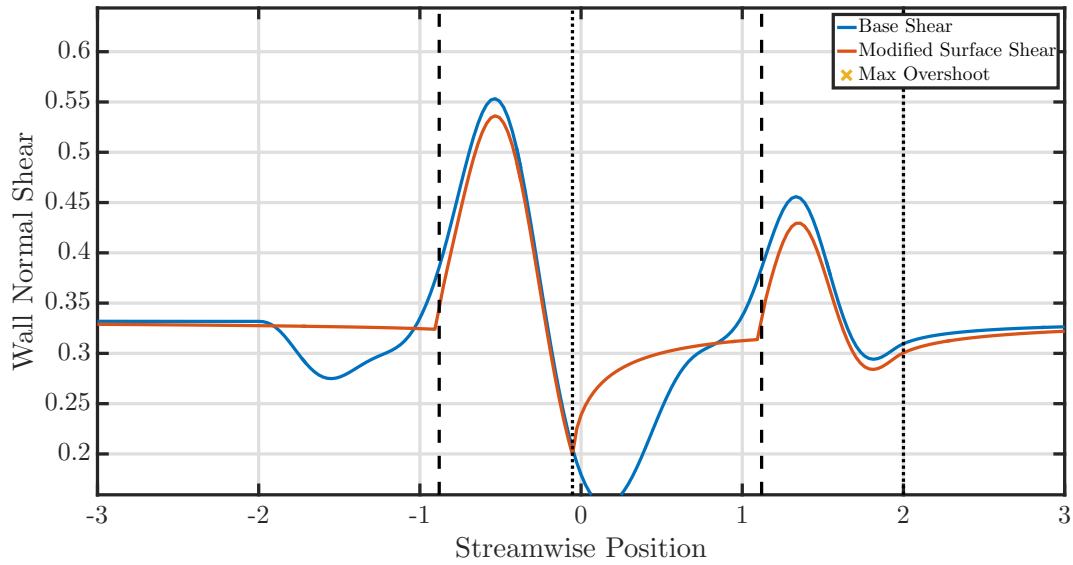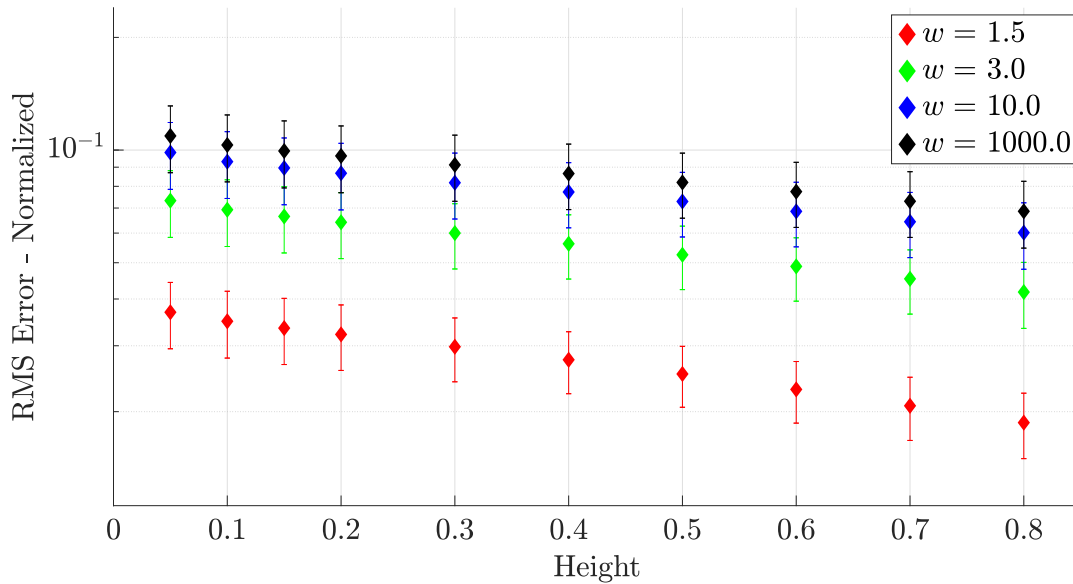
Figure 5.7: Example of no-slip results.

Figure 5.8: RMS error for no-slip (normalized by the range of shear stress measured in the control configuration)
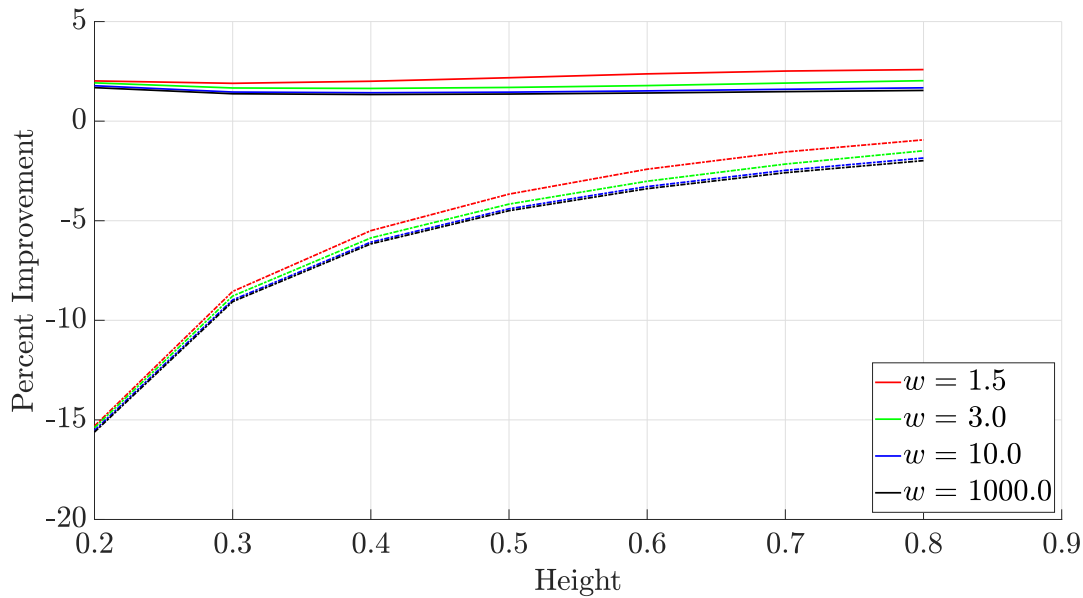
Figure 5.9: Percent improvement in RMS error for no-slip, effective surface height held constant. Solid lines are normalized, dashed lines are unnormalized.

surface and the real geometry increases.

Holding ω constant as the heights increased resulted in a steady improvement of relative error (shown as solid lines in figure 5.9). The model got better for all effective surfaces, although there is a difference in how fast they improved. However, unnormalized results (shown as dashed lines in figure 5.9) show this improvement is only relative to how fast the range of shear stress is increasing. Without the normalizing factor, there is a large deterioration in results, particularly at low heights. Removing the effect of the increase in shear stress range shows the absolute undershoot error increases (shown in figure 5.10). No-slip is the only case where trends completely reverse absent a normalizing factor. At the heights simulated, there is no way to match the control values without an offsetting boundary condition.

While no-slip performed better than no-shear in terms of RMS error, the large dependence on effective surface height is undesirable. Additionally, although the model improved relative to the the range in shear stress, increasing the height of the roughness made the absolute error worse.
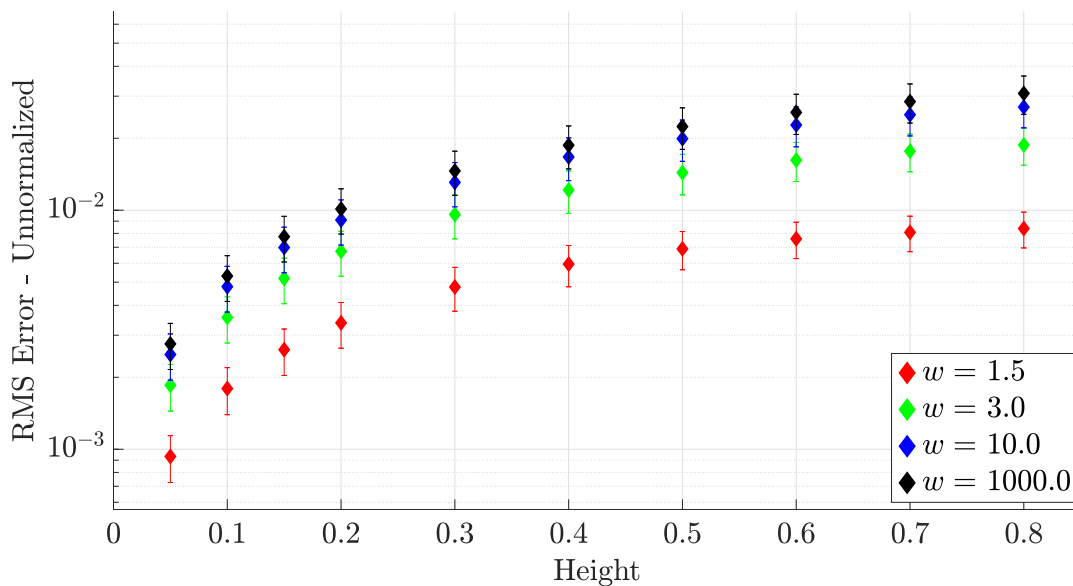
Figure 5.10: RMS error for no-slip (unnormalized)

5.3 Imposed-Slip Effective Surface Boundary Conditions

The following results examine geometries where an imposed slip velocity is applied at the effective surface. The order of magnitude of E_{RMS} for imposed-slip is comparable to no-slip, although results vary more. Imposed-slip initially shows large improvement as the height of the geometries increased, although this slows or reverses at the taller geometries. Additionally, this model gave a large spread of results among the 100 geometries tested; standard deviations ranged from $30 - 70\%$ of the mean values. Figure 5.11 shows how the normalized RMS error changes as the height of the roughness increases. All effective surfaces improve until a height of 0.4, after which the relative error increases for all but the lowest effective surface. A similar trend is shown in the unnormalized data in figure 5.12, where all effective surfaces begin to worsen at some point.
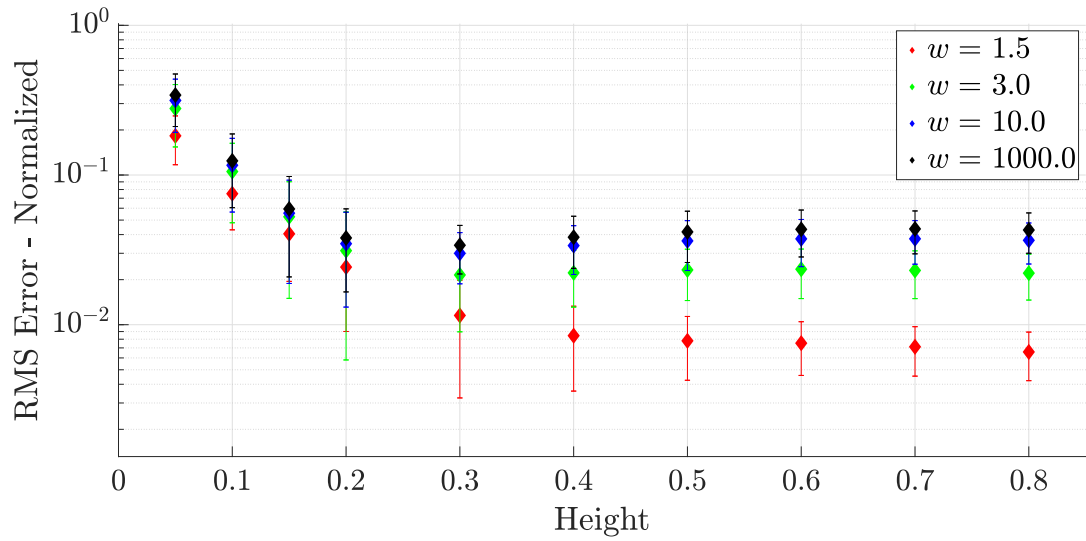
Figure 5.11: RMS error for imposed-slip (normalized by the range of shear stress measured in the control configuration)
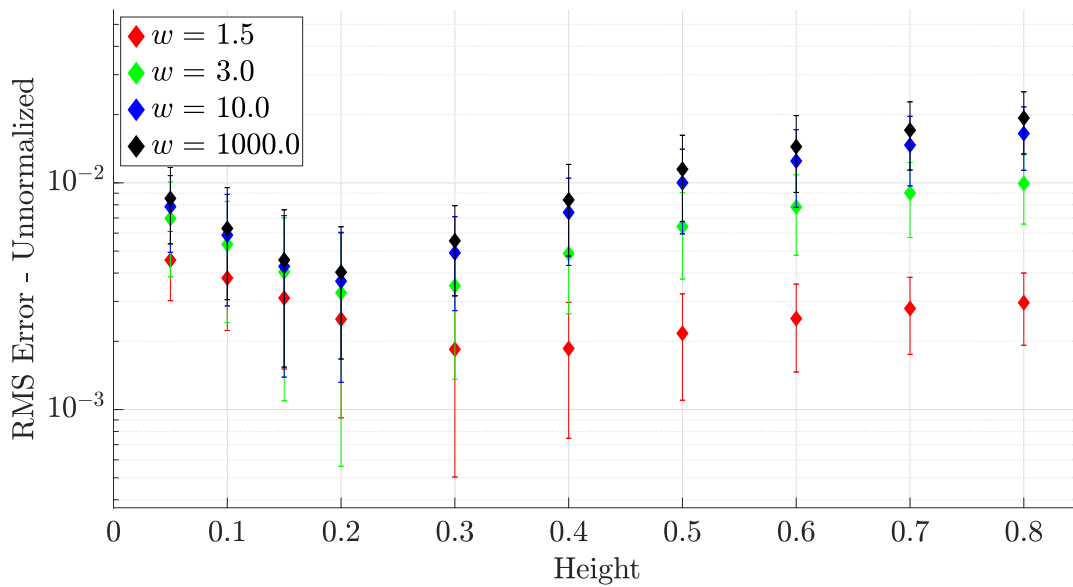

Figure 5.12: RMS error for imposed-slip (unnormalized)

The impact of effective surface selection is dependent on the height of the roughness. At lower
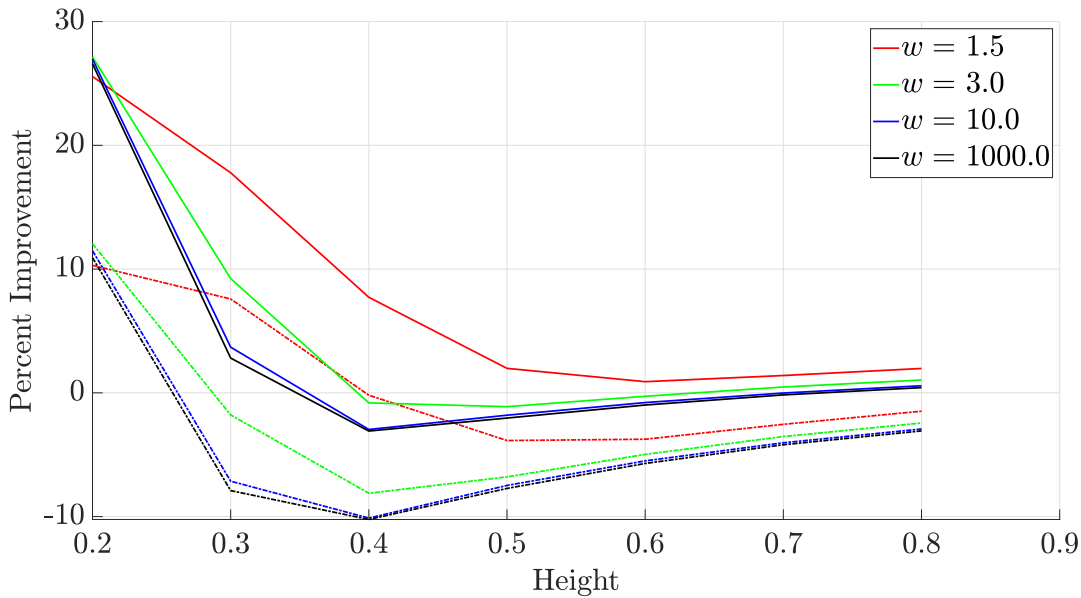
Figure 5.13: Percent improvement in RMS error for imposed-slip, effective surface height held constant. Solid lines are normalized, dashed lines are unnormalized.

heights, influence is small ($\sim 20\% - 50\%$ difference between $\omega = 1.5, 1000$), however as the height of the geometry increases, the impact of surface choice grows quickly (up to $\sim 120\%$). Holding ω constant and increasing geometry height (figure 5.13) again emphasizes a trend reversal at $h = 0.4$. The change in error appears to stabilize near a small percent change (either positive or negative) as the roughness gets larger. This stabilization is certainly a result of the balance of terms used to determine the maximum slip velocity, which will be discussed later.

Moving to RMS overshoot, figure 5.14 shows how as the height of the roughness increases, the mean overshoot continually decreases. The lowest effective surface shows the slowest improvement in overshoot error (shown in figure 5.15), being outperformed at steep geometries by higher effective surfaces. This slow decrease in overshoot error explains why the reversal in E_{RMS} trends is delayed to a higher geometry height. For all other effective surfaces past a height of $h = 0.4$, the majority of error is undershoot error, which increases with the height of the roughness. The model, which begins at low heights over-predicting shear stress on exposed segments of geometry, switches at higher heights to under-predicting shear stress. It is apparent that the rate of change in
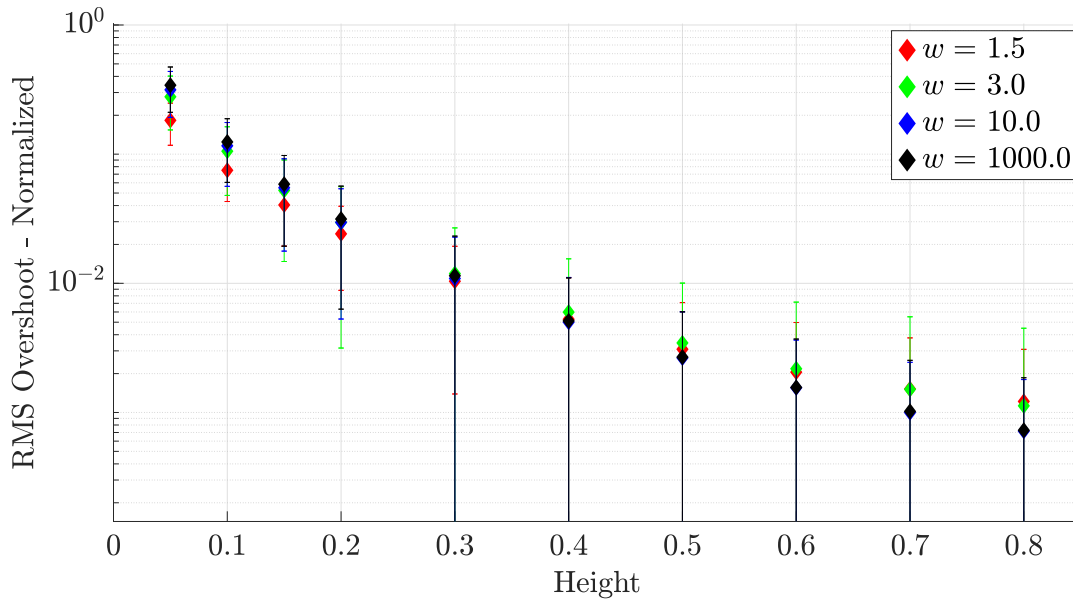
Figure 5.14: RMS overshoot for imposed-slip (normalized by the range of shear stress measured in the control configuration)

guessed $u_{r,max}$ is not correctly matched to the needed rate of change in this model.

Trends are very similar for maximum overshoot (figures 5.16 and 5.17), although there is no consistent location for maximum overshoot as in the no-shear models. Figure 5.18, an example of a close match to control results, demonstrates this fact. Linearly ramping the slip velocity back to the no-slip condition is beneficial for avoiding the large spike in shear stress. However, some configurations did still show this effect.
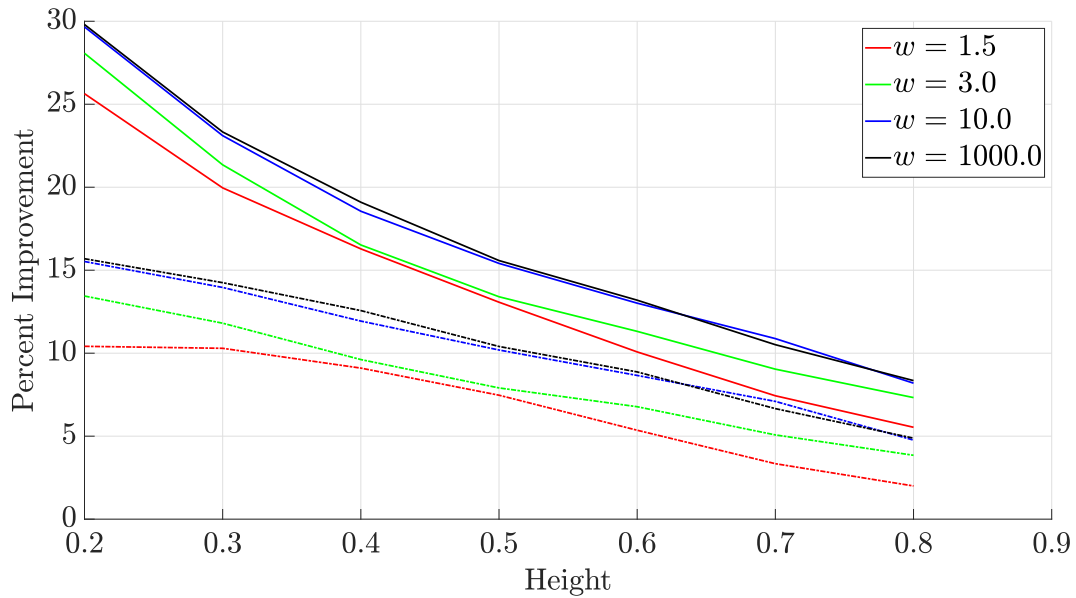
Figure 5.15: Percent improvement in RMS overshoot for imposed-slip, effective surface height held constant. Solid lines are normalized, dashed lines are unnormalized.

Figure 5.16: Maximum overshoot for imposed-slip (normalized by the range of shear stress measured in the control configuration)

Figure 5.17: Percent improvement in maximum overshoot for imposed-slip, effective surface height held constant. Solid lines are normalized, dashed lines are unnormalized.
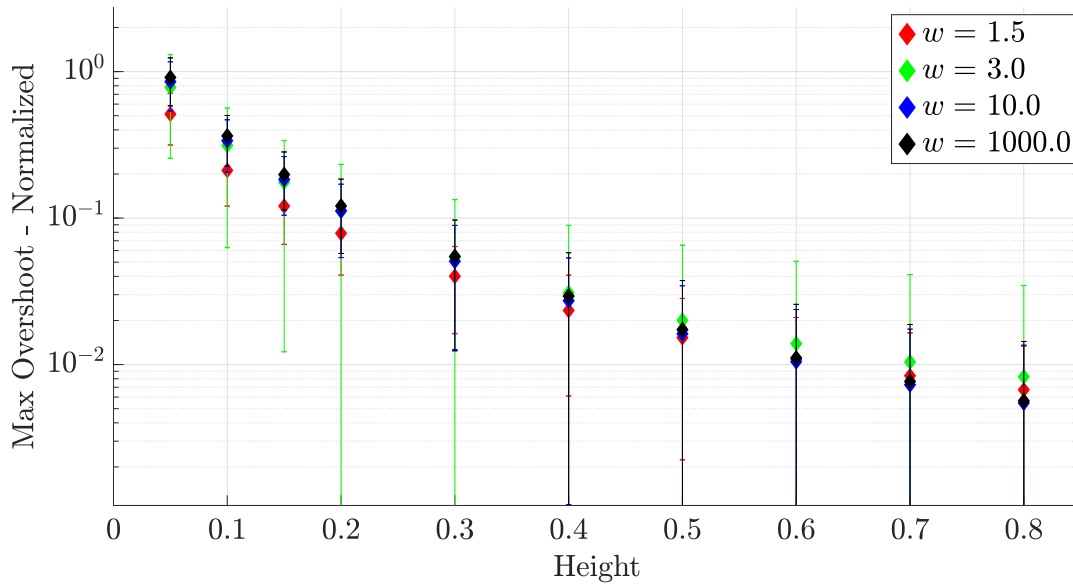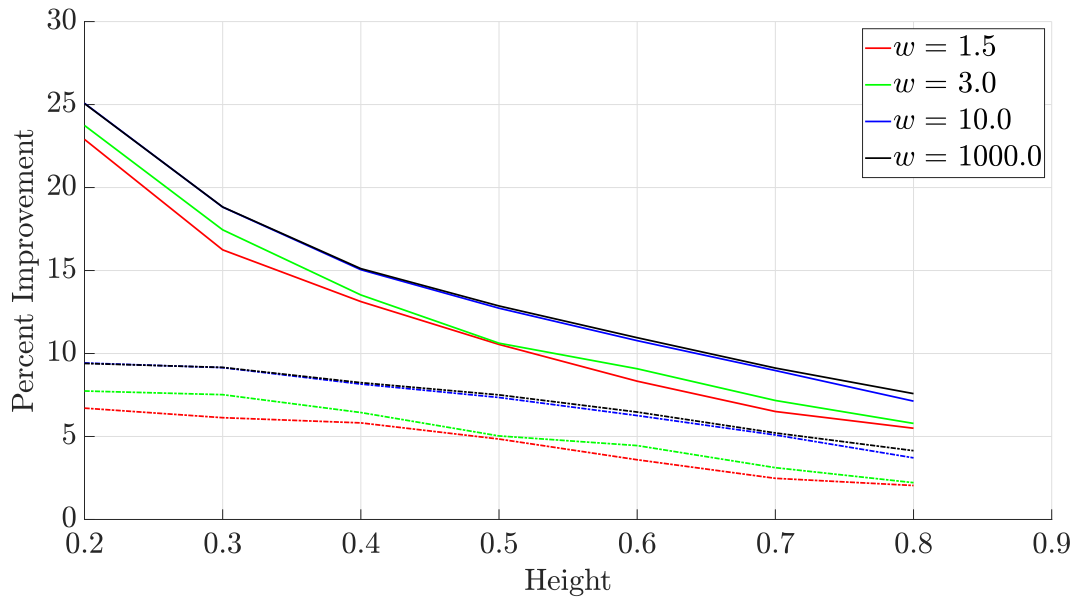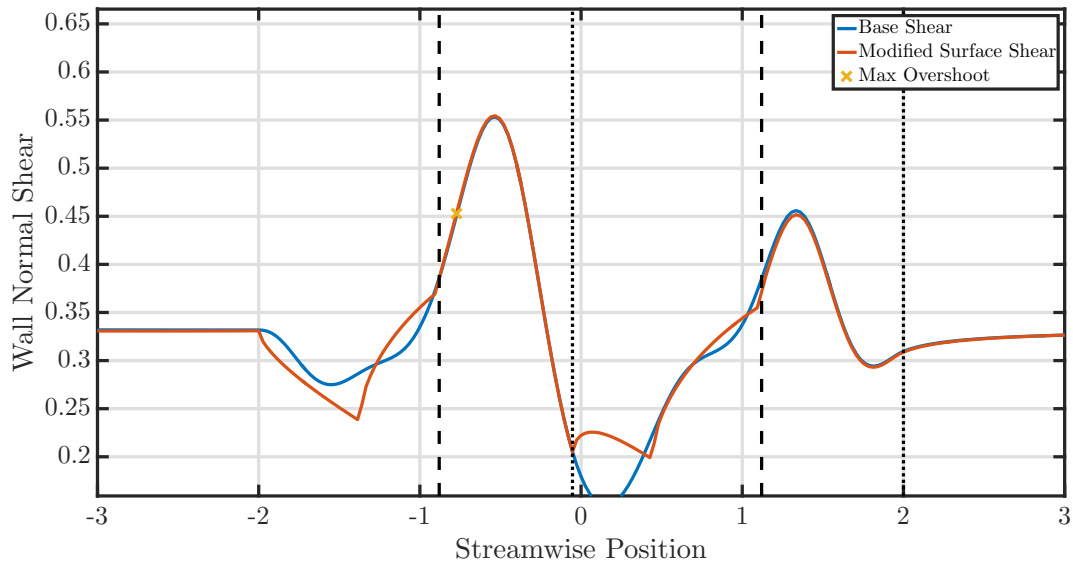

Figure 5.18: Example of imposed-slip results.

In section 2, it was described how a previous DNS [13] seems to indicate the importance of

matching in-plane velocity when an effective surface in imposed. The following measurements will quantify how closely the recirculation model described the in-plane velocity. Three heights ($h = 0.1, 0.3, 0.5$) were selected to output full velocity data for the control roughness configurations. These heights were selected in particular because they bound the trend reversal seen in the statistical data. To extract the in-plane velocity, the coordinates for the effective surface heights were used to define a line to interpolate full velocity data along. Figure 5.19 illustrates this: the contours represent velocity magnitudes calculated when simulating the control roughness configuration. The black line represents an effective surface geometry. Both u and v are interpolated along this line, then the velocity vector is projected onto the effective surface. This gives the correct control in-plane velocity.
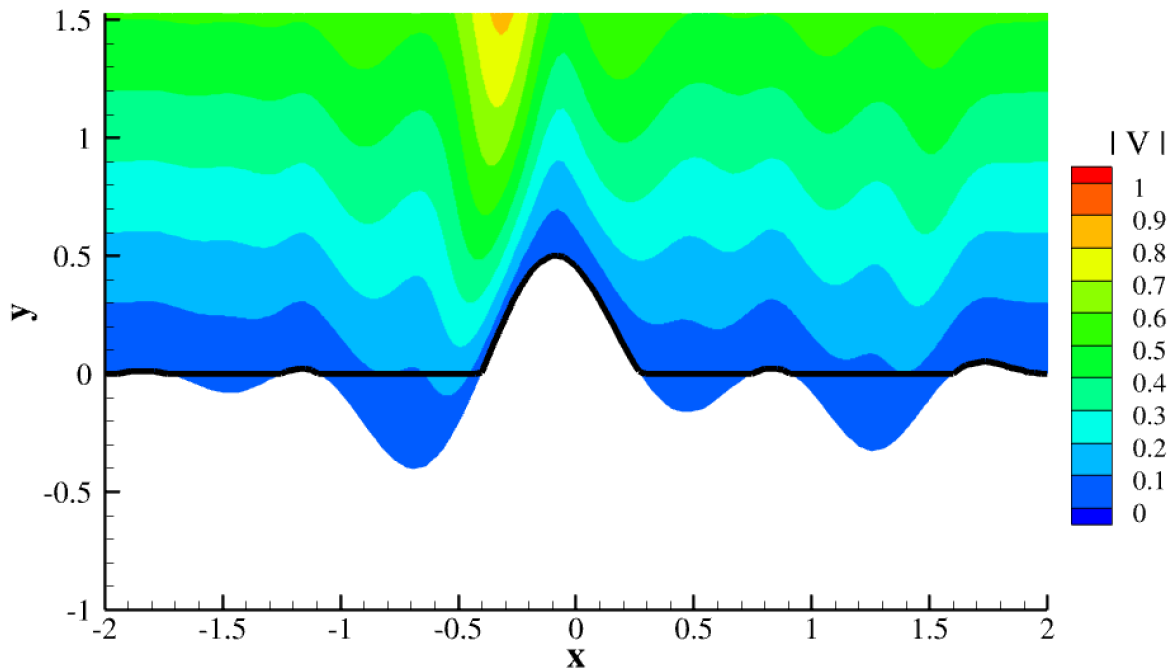
Figure 5.19: Example showing how true in-plane velocity was extracted from the control data.

The maximum velocity error was then defined as the absolute difference between the maxi-
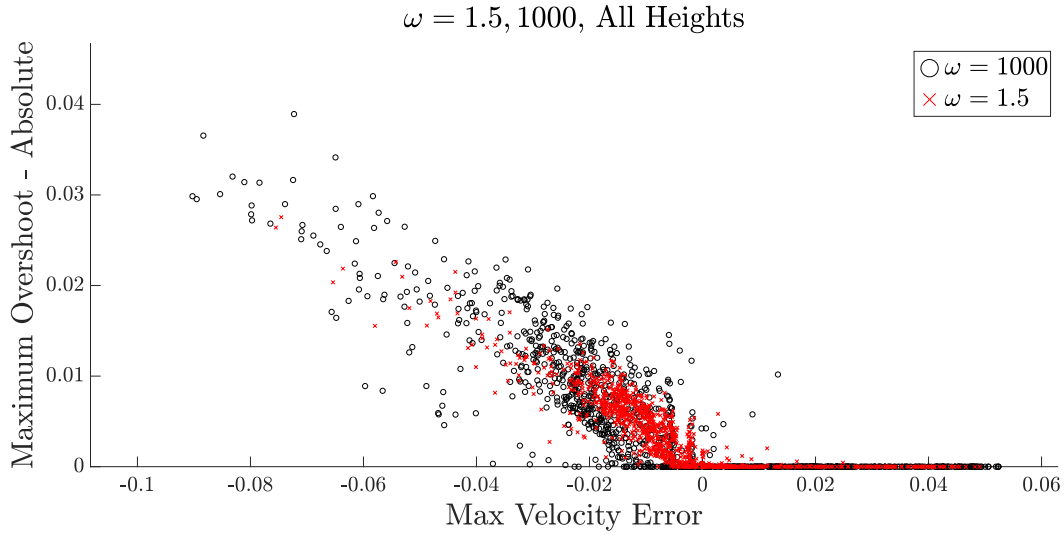
Figure 5.20: Correlation between error in in-plane velocity and the maximum absolute overshoot in shear stress.

mum true in-plane velocity, and the maximum recirculation velocity prescribed by the imposed-slip model. This velocity error is compared against the shear stress error measured only on the following exposed roughness peak. Plotting these two values reveals a correlation shown in figure 5.20. Overestimating slip velocity clearly resulted in overshoot error. Once the model began imposing a lower maximum slip velocity than actually would appear at that effective surface height, the model began to undershoot the shear stress upon return to the no-slip condition at the exposed geometry.
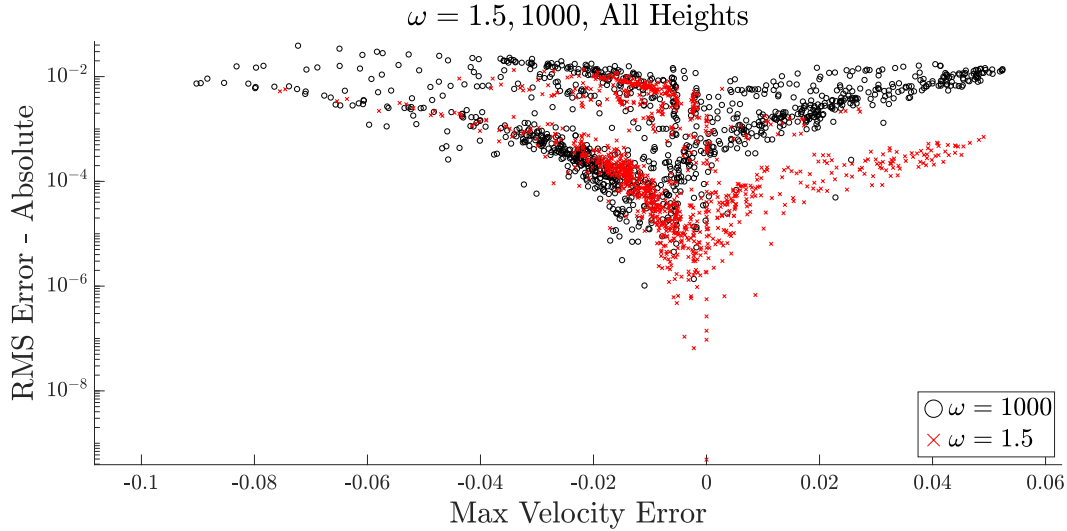
Figure 5.21: Correlation between error in in-plane velocity and the absolute RMS error.

Figure 5.21 shows a v-shape channeling towards zero slip velocity error; E_{RMS} left of the dip is primarily the result of overshoot error, while right of the dip it is primarily the result of undershoot error. There is a noticeable offset between the v-shapes for $\omega = 1.5, 1000$. The explanation for this offset most likely lies on the difference in geometry shape. Recall that the pressure gradient is simultaneously determined with all other flow variables, and also that it is a global quantity. Referring back to equation 4.2, it is evident that the pressure is reliant on the derivative of the geometry. Obviously, there is a large difference between the derivatives for $\omega = 1.5$ and 1000, and again between the effective surfaces and the real geometry. Although the slip velocity attempts to offset the change in geometry, the displacement term is usually an order of magnitude smaller that the geometry derivative, and so there remains an error.

To investigate more about why E_{RMS} trends reversed when they did, the comparison was broken up based on the height of the roughness (shown in figure 5.22). These results explain why the $h = 0.3$ case general performed the best; the $u_{r,max}$ was nearest the actual in-plane velocity. The simplified model chosen for max velocity resulted in the closest match to the actual velocity at that effective surface height. For the lowest effective surface, the shape of the enclosed area does not change rapidly as the height of the roughness is increased, therefore the modeled maximum slip
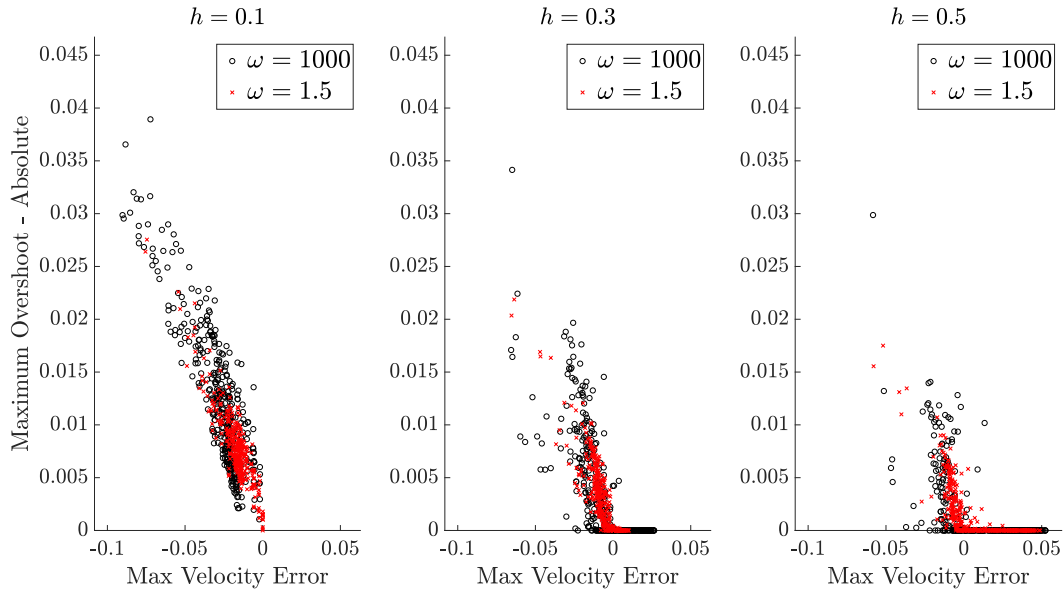
49

Figure 5.22: Correlation between error in in-plane velocity and the maximum absolute overshoot.

velocity cannot change rapidly either. This explains the slow improvement of the lowest effective surface, as well as the tighter data.

Despite the difficulty in exactly matching the pressure due to the change in geometry, the imposed-slip model performs well, even using the simplistic model prescribed here. The modeled maximum slip velocity is primarily balanced between two characteristics of the enclosed, 'recirculating' airspace: the depth of the enclosed area and the relative distribution of the enclosed area (modeled via I_{yy}/I_{xx}). The exchange between overshoot and undershoot error indicates the balance between these two terms is not yet perfect and resulted in a large spread of results. However, these results demonstrate that imposed-slip has the ability to closely model distributed roughness using an effective surface.

5.4 Shielding Effect

The model created using an effective surface must not only match distributed roughness results, it should replicate shielding, where small amplitude roughness reduced the effect of larger elements. As a small proof of concept, the shielding effect is tested using the imposed-slip model
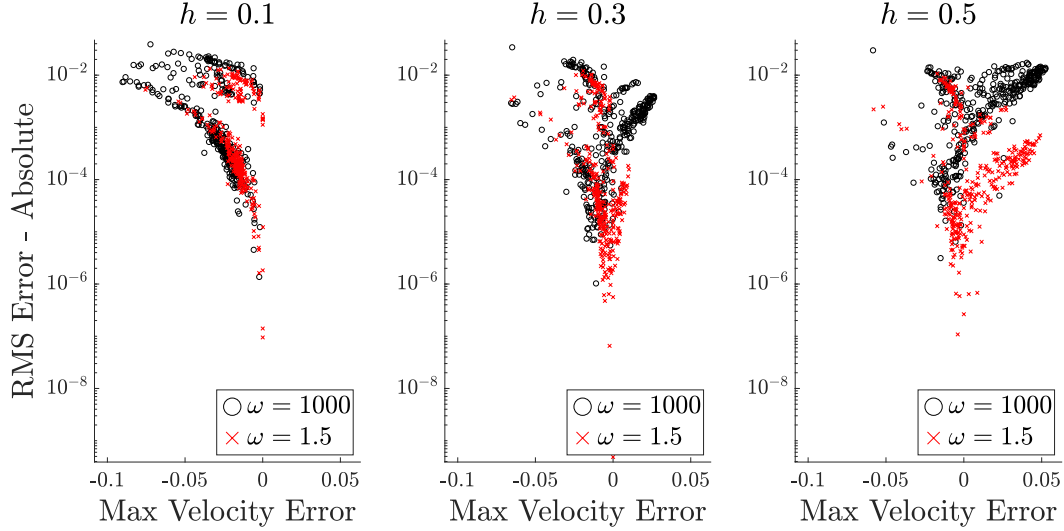
50

Figure 5.23: Correlation between error in in-plane velocity and the absolute RMS error.

built for this thesis. A large, 2D 'DRE' is placed among the roughness, using Smith's original geometry shifted to the center of the distributed roughness patch [32].

$$F(x)_{DRE} = h_D(x^2 - 0.25) \tag{5.3}$$

Distributed roughness is placed around the DRE in the usual manner (shown in figure 5.24). An effective surface is then applied to the distributed roughness. The DRE-only case is run as a control configuration, and the modeled shear stress from the DRE with distributed roughness is compared against those results. The shear stress results are shown in figure 5.25 from the control (DRE only) configuration, and the modeled distributed roughness, along with the 'true' distributed roughness case without an effective surface applied.

There are two indicators that transition would be less likely in such a scenario. First, the maximum shear stress, which occurs for both cases slightly in front of the top of the bump, is less in the presence of distributed roughness. Second, the large drop in shear stress following the bump, which for large bumps can lead to separation behind the element, is significantly reduced by the roughness. Both of these improvements can be tied to the presence of small pieces of

51
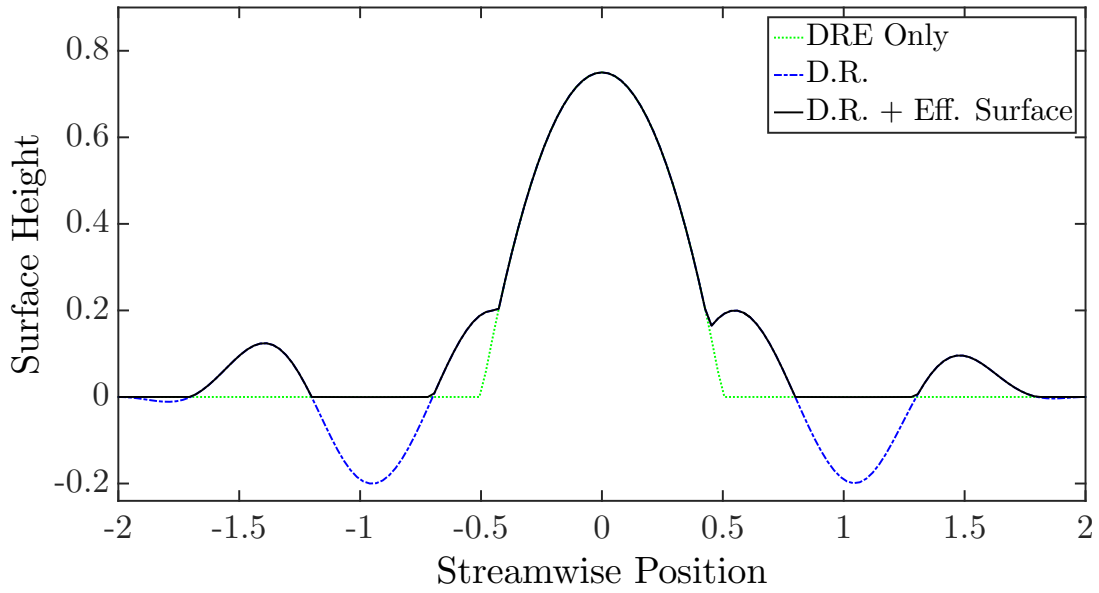
Figure 5.24: Geometry for 'shielding' configuration
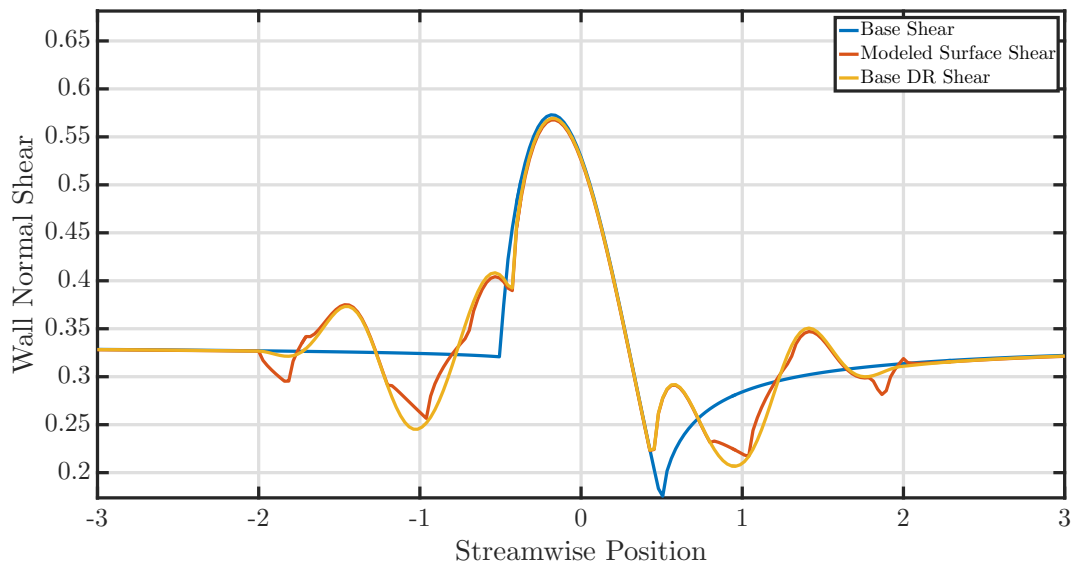
Figure 5.25: Resulting shear stress after applying distributed roughness with an effective surface around a 'DRE'.

distributed roughness immediately in front and behind the DRE, reducing the apparent height of the roughness.

While these results are promising, they are unsurprising. The distributed roughness both ahead and behind the DRE easily modifies the apparent height of the roughness. However, experimentally, a field of roughness can lessen the effect of a DRE even when the geometry in the immediate vicinity may not actually affect the height of the DRE (offset the geometric surface from the $y = 0$ plane). However, these results are encouraging that the effective surface model may be able to capture the shielding effect.

6. CONCLUSIONS

The evaluation of the effective surface models considers the ability to predict the wall shear stress for a large range in roughness configurations. The influence of effective surface shape, although more apparent in some boundary conditions than others, always affected results. This, as mentioned in the context of the imposed-slip model, was due to the dependance of pressure on geometry slope. The boundary conditions presented here are intended to offset this geometry change. The results of this study provide evidence on why certain boundary conditions performed better than others.

The first boundary condition, no-shear, was the inspiration for this study. Judging by past experiments that showed negligible effect from negative geometry, we hypothesized that fluid below the effective surface has very little effect on the boundary layer. To capture this notion, a no-shear condition was enforced at the effective surface boundary. Results conclusively showed this could not replicate control results. Enforcing no-shear allows fluid near the wall to accelerate to large speeds very close to the roughness. This, in effect, allows higher momentum fluid to move closer to the roughness peaks, exacerbating their effect on the flow. The dramatic spike in shear stress upon return to no-slip at exposed geometry is indicative of a large streamwise gradient enforced on fluid particles at the wall. This gradient propagates in the normal direction, causing large normal gradients to form as well. Additionally, the fluid does not fully recover before returning to a no-shear condition over another effective surface. Consequently, all error is overshoot error, contrary to the other two conditions. The results of this study conclusively show that no-shear is *not* the correct boundary condition to enforce on an effective surface.

The next boundary condition, no-slip, is inspired by experiments that consider sandpaper-like roughness. Sandpaper-like roughness is characterized by completely random, tightly packed, sharp elements. Measurements over these surfaces by a number of investigators have shown how the measured boundary layer profiles are similar to a Blasius boundary layer profile, displaced outward from the geometric surface. Implementing this condition over the roughness presented in this

study shows the error only decreases relative to the growth in range of shear stress. Admittedly, the roughness presented in this study, due to the geometry restrictions of triple-deck theory, is not similar to sandpaper roughness.

A strong argument for why the no-slip condition may exist for more extreme roughness is the possibility of pockets of trapped, static fluid forming between roughness peaks. In this study, height restrictions were intentionally created to suppress any separation bubbles. Without those pockets of fluid, raising the effective surface away from the geometry but maintaining a no-slip condition simulated less severe geometry. The results of this study cannot guide hypotheses about the success of no-slip conditions for extreme geometry, because the parameter space examined here is too shallow. However, it is conclusive that no-slip has limited usefulness for more mild roughness, indicating this boundary condition cannot encompass the full parameter space.

The final boundary condition presented, imposed-slip, shows mixed results. While, on average, only one of the effective surfaces continually performed the best overall in terms of RMS error in wall shear stress results, the large spread in results did allow some control geometric configurations to be near perfectly matched by the imposed-slip model. Undoubtedly, the slip velocity model prescribed had a large impact on the trends shown by this study. Closer investigation into local results reveals a strong dependence on the accuracy of the prescribed u_{max}. Models which showed large success in the RMS error results very nearly matched the actual u_{max} the flow would experience at the location of the effective surface.

A very similar result was presented by Drews [13] where the valleys were replaced by a slip surface at $y = 0$. Velocity results from this DNS study closely matched the in-plane velocity results from the full DNS case. Velocity perturbations downstream of the reduced roughness case closely matched the velocity perturbations from the full roughness case. These results, in conjunction with the results presented here, suggest an important parameter to match over the effective surface is the velocity magnitude.

These results also shed more light on the other two boundary conditions. While certainly a large portion of the no-shear model's spike in wall shear stress resulted from the sudden imposition of

no-slip, the fact that the shear stress continued to overshoot over the rest of the exposed geometry resembles the cases of the imposed-slip model that dramatically over-predicted the u_{max} velocity. Similarly, the no-slip model dramatically under-predicts the u_{max} velocity and so under-predicts shear stress continually.

As a reminder of this study's overall motivation, the goal is to create a reduced-order distributed roughness model to allow for easier, less expensive studies of roughness, as well as insight into how laminar flow interacts with distributed roughness. Three goals for the final model were laid out. It would:

1. correctly predict boundary layer quantities above the effective surface, where the highest peaks in the roughness field remain exposed.

2. be capable of handling arbitrary, rough, 3D surfaces.

3. handle the analysis of any roughness patch with significantly less computational cost than a DNS of the same field.

While the triple-deck model used for this study clearly completed item 3 above, it is not a tenable option for extreme geometry roughness, due to the strict scaling limitations on the roughness. This restricts the model presented here from succeeding at item 2 listed above. Future studies should explore different simulation options.

The main focus of this study addressed the first topic. A change in geometry, coupled with a new boundary condition over the effective surfaces, was examined for its ability to replicate wall shear stress over 2D exposed geometry, evaluated using a triple-deck model. The results of this study suggest pursuing an imposed-slip model, refined to better reflect velocity trends in the areas where an effective surface would be applied. This presents a clear path for future research, where detailed investigation into the velocity contained among the distributed roughness could be closely examined.

REFERENCES

[1] M. V. Morkovin, E. Reshotko, and T. Herbert, "Transition in open flow systems - a reassessment.," *Bull. Am. Phys. Soc.*, 1994.

[2] M. Napolitano, M. J. Werle, and R. T. Davis, "Numerical technique for the triple-deck problem," *AIAA Journal*, vol. 17, no. 7, pp. 699–705, 1979.

[3] E. Reshotko, "Transient growth: A factor in bypass transition," *Physics of Fluids*, vol. 13, no. 5, pp. 1067–1075, 2001.

[4] I. Tani, "Boundary-layer transition," *Annual Review of Fluid Mechanics*, vol. 1, no. 1, pp. 169–196, 1969.

[5] M. V. Morkovin, *On Roughness — Induced Transition: Facts, Views, and Speculations*. New York, NY: Springer US, 1990.

[6] M. T. Landahl, "A note on an algebraic instability of inviscid parallel shear flows," *Journal of Fluid Mechanics*, vol. 98, no. 2, p. 243âĂŞ251, 1980.

[7] K. Singh and J. L. Lumley, "Effect of roughness on the velocity profile of a laminar boundary layer," *Applied Scientific Research*, vol. 24, pp. 168–186, Dec 1971.

[8] L. Leventhal and E. Reshotko, "Preliminary experimental study of disturbances in a laminar boundary layer due to distributed surface roughness," *AIAA Paper 81-1224*, 1981.

[9] J. M. Kendall, "Laminar boundary layer velocity distortion by surface roughness: Effect upon stability," *AIAA Paper 81-0195*, 1981.

[10] M. Tadjfar, E. Reshotko, A. Dybbs, and R. V. Edwards, "Velocity measurements within boundary layer roughness using index matching," 11 1985.

[11] T. C. Corke, A. Bar Sever, and M. V. Morkovin, "Experiments on transition enhancement by distributed roughness," *The Physics of Fluids*, vol. 29, no. 10, pp. 3199–3213, 1986.

[12] R. S. Downs, E. B. White, and N. Denissen, "Transient growth and transition induced by random distributed," *AIAA Journal*, vol. 46, no. 2, pp. 451–462, 2008.

[13] S. D. Drews, "Direct numerical simulations of flow past quasi-random distributed roughness," Master's thesis, University of Texas, 5 2012.

[14] M. S. Kuester and E. B. White, "Roughness receptivity and shielding in a flat plate boundary layer," *Journal of Fluid Mechanics*, vol. 777, pp. 430–460, 2015.

[15] M. N. McMillan, A. R. Berger, and E. B. White, "Measurements of distributed roughness receptivity," *AIAA Paper 2017*, 2017.

[16] F. G. Ergin and E. B. White, "Unsteady and transitional flows behind roughness elements," *AIAA Journal*, vol. 44, no. 11, 2006.

[17] M. Gaster, "Understanding the effects of surface roughness on the growth of disturbances," 2016.

[18] K. Stewartson and P. Williams, "Self-induced separation," *Proc. R. Soc. Lond.*, vol. A312, no. 181, 1969.

[19] V. Y. Neiland, "Theory of laminar boundary layer separation in supersonic flow," *Fluid Dynamics*, vol. 4, pp. 33–35, Jul 1969.

[20] A. Messiter, "Boundary-layer flow near the trailing edge of a flat plate," *SIAM Journal on Applied Mathematics*, vol. 18, no. 1, pp. 241–257, 1970.

[21] R. E. Meyer, "A View Of The Triple Deck," *Siam Journal On Applied Mathematics*, vol. 43, no. 4, pp. 639–663, 1983.

[22] S. Goldstein, "On Laminar Boundary Layer Flow Near A Position Of Separation," *The Quarterly Journal of Mechanics and Applied Mathematics*, vol. 1, pp. 43–69, 01 1948.

[23] A. E. P. Veldman, "Matched asymptotic expansions and the numerical treatment of viscous-inviscid interaction," *Journal of Engineering Mathematics*, vol. 39, pp. 189–206, Mar 2001.

[24] L. Rosenhead, ed., *Laminar Boundary Layers*. Oxford University Press, 1963.

[25] A. P. Rothmayer and F. T. Smith, *The handbook of fluid dynamics*. CRC Press LLC, 1998.

[26] F. T. Smith, P. W. M. Brighton, P. S. Jackson, and J. C. R. Hunt, "On boundary-layer flow past two-dimensional obstacles," *Journal of Fluid Mechanics*, vol. 113, pp. 123–152, 1981.

[27] J. Tsao and A. Rothmayer, "Application of triple-deck theory to the prediction of glaze ice roughness formation on an airfoil leading edge," *COMPUTERS & FLUIDS*, vol. 31, pp. 977–1014, NOV 2002.

[28] A. E. P. Veldman, "The calculation of incompressible boundary layers with strong viscous-inviscid interaction," *NASA STI/Recon Technical Report N*, vol. 81, aug 1980.

[29] H. Pletcher., R., C. Tannehil, J., and A. Anderson, D., *Computational Fluid Mechanics and Heat Transfer*. CRC Press LLC, 2013.

[30] V. V. Sychev, A. I. Ruban, V. V. Sychev, and G. L. Korolev, *Asymptotic Theory of Separated Flows*. Cambridge University Press, 1998.

[31] W. H. Press, S. A. Teukolsky, W. T. Vetterling, and B. P. Flannery, *Numerical Recipes 3rd Edition: The Art of Scientific Computing*. New York, NY, USA: Cambridge University Press, 3 ed., 2007.

[32] F. T. Smith, "Laminar flow over a small hump on a flat plate," *Journal of Fluid Mechanics*, vol. 57, pp. 803–824, 1973.

[33] I. J. Sobey, *Introduction to Interactive Boundary Layer Theory*. Oxford University Press, 2000.

[34] R. I. Sykes, "Stratification effects in boundary layer flow over hills," *Proceedings of the Royal Society of London. A. Mathematical and Physical Sciences*, vol. 361, no. 1705, pp. 225–243, 1978.

[35] A. Reyhner, T. and I. Flügge-Lotz, "The interaction of a shock wave with a laminar boundary layers," *International Journal of Non-Linear Mechanics*, vol. 3, no. 2, pp. 173 – 199, 1968.